NASA TECHNICAL NOTE

NASA TN D-6909

NASA TN D-6909

DYNAMIC STABILITY DERIVATIVES AT ANGLES OF ATTACK FROM -5° TO 90° FOR A VARIABLE-SWEEP FIGHTER CONFIGURATION WITH TWIN VERTICAL TAILS

by Sue B. Grafton and Ernie L. Anglin

Langley Research Center
Hampton, Va. 23365

NATIONAL AERONAUTICS AND SPACE ADMINISTRATION • WASHINGTON, D. C. • OCTOBER 1972

1. Report No.	2. Government Accession No.	3. Recipient's Catalog No.
NASA TN D-6909		

4. Title and Subtitle	5. Report Date
DYNAMIC STABILITY DERIVATIVES AT ANGLES OF ATTACK FROM -5° TO 90° FOR A VARIABLE-SWEEP FIGHTER CONFIGURATION WITH TWIN VERTICAL TAILS	October 1972
	6. Performing Organization Code

7. Author(s)	8. Performing Organization Report No.
Sue B. Grafton and Ernie L. Anglin	L-8426
	10. Work Unit No.
9. Performing Organization Name and Address	501-17-01-06
NASA Langley Research Center Hampton, Va. 23365	11. Contract or Grant No.
	13. Type of Report and Period Covered
12. Sponsoring Agency Name and Address	Technical Note
National Aeronautics and Space Administration Washington, D.C. 20546	14. Sponsoring Agency Code

15. Supplementary Notes

16. Abstract

An investigation was conducted in the Langley full-scale tunnel to determine the dynamic stability derivatives in pitch, roll, and yaw over an angle-of-attack range of -5° to 90° for a variable-sweep fighter configuration with twin vertical tails. The study consisted of forced-oscillation tests of a 1/10-scale model of the airplane at a Reynolds number of 0.4×10^6 based on the reference wing mean aerodynamic chord. Tests were conducted for wing sweep angles of 22°, 35°, 50°, and 68°, and the effects of the vertical and horizontal tails, wing leading-edge slats, nose-mounted canards, and frequency of the oscillation were also evaluated.

17. Key Words (Suggested by Author(s))	18. Distribution Statement
Dynamic stability Fighter airplane High angles of attack	Unclassified – Unlimited

19. Security Classif. (of this report)	20. Security Classif. (of this page)	21. No. of Pages	22. Price*
Unclassified	Unclassified	51	$3.00

*For sale by the National Technical Information Service, Springfield, Virginia 22151

DYNAMIC STABILITY DERIVATIVES AT ANGLES OF ATTACK FROM -5° TO 90° FOR A VARIABLE-SWEEP FIGHTER CONFIGURATION WITH TWIN VERTICAL TAILS

By Sue B. Grafton and Ernie L. Anglin
Langley Research Center

SUMMARY

An investigation was conducted in the Langley full-scale tunnel to determine the dynamic stability derivatives in pitch, roll, and yaw over an angle-of-attack range of -5° to 90° for a variable-sweep fighter configuration with twin vertical tails. The data obtained in the tests are intended to serve as inputs for theoretical analysis of the stall and spin characteristics of the airplane. The study consisted of forced-oscillation tests of a 1/10-scale model of the airplane at a Reynolds number of 0.4×10^6 based on the reference wing mean aerodynamic chord; the static tests were run at a Reynolds number of 0.5×10^6. Tests were conducted for wing sweep angles of 22°, 35°, 50°, and 68°, and the effects of the vertical and horizontal tails, wing leading-edge slats, nose-mounted canards, and frequency of the oscillation were also evaluated.

The results of the investigation showed that the model had stable values of damping in pitch, roll, and yaw over the entire angle-of-attack range below the stall for all wing-sweep angles. Large reductions in damping in pitch occurred near maximum lift. At angles of attack approaching 90°, unstable values of damping in yaw were measured. The unstable values of yaw damping were caused by aerodynamic phenomena produced by flow over the fuselage forebody at high angles of attack. Stable values of yaw damping were obtained when canards were added to the fuselage forebody of the model.

INTRODUCTION

The National Aeronautics and Space Administration is currently engaged in a research program to develop and validate theoretical methods for prediction of airplane stall and spin characteristics. A major portion of this program involves correlation between theoretical calculations and data obtained by free-flight tests using dynamically scaled radio-controlled models of several fighter airplane configurations.

The present investigation was conducted to measure the dynamic stability derivatives of a current variable-wing-sweep fighter configuration over the angle-of-attack range normally associated with spinning. These data are intended to serve as aerodynamic inputs

for theoretical studies of the stall and spin characteristics of this particular configuration. The investigation consisted of forced-oscillation tests which were conducted over an angle-of-attack range from -5° to 90° for wing sweep angles of 22°, 35°, 50°, and 68°. Tests were also conducted to determine the effects of the horizontal and vertical tails, wing leading-edge slats, canard surfaces on the fuselage forebody, and the frequency of the oscillation. In order to aid in the interpretation of the dynamic data, a limited amount of data on the static longitudinal and lateral-directional aerodynamic characteristics of the model were also determined and are presented herein.

SYMBOLS

The longitudinal and lateral-directional data presented herein are referred to the body-axis system. (See fig. 1.) All static force test data are referred to a moment center located at 16.25 percent of the mean aerodynamic chord of the wing for a sweep angle of 20°, and all dynamic force test data are referred to 31.55 percent of this mean aerodynamic chord. There were no significant changes in the dynamic force test data when they were transferred to 16.25 percent of the mean aerodynamic chord; therefore, all data are presented as measured. In order to facilitate international usage of data presented, dimensional quantities are presented both in the International System of Units (SI) and in the U.S. Customary Units. Measurements were made in U.S. Customary Units and equivalent dimensions were determined by using the conversion factors given in reference 1.

b	wing span, based on wing sweep angle of 20°, m (ft)
c	local chord, m (ft)
$\bar{c}$	mean aerodynamic chord, based on wing sweep angle of 20°, m (ft)
F_A	axial force, N (lb)
F_D	drag force, N (lb)
F_L	lift force, N (lb)
F_N	normal force, N (lb)
F_Y	side force, N (lb)
f	frequency of oscillation, hertz
i_t	tail incidence, deg

k	reduced-frequency parameter, $\omega b/2V$ for lateral-directional parameter or $\omega \bar{c}/2V$ for longitudinal parameter
M_X	rolling moment, m-N (ft-lb)
M_Y	pitching moment, m-N (ft-lb)
M_Z	yawing moment, m-N (ft-lb)
p	rolling velocity, rad/sec
q	pitching velocity, rad/sec
q_∞	free-stream dynamic pressure, $\frac{1}{2}\rho V^2$, N/m^2 (lb/ft^2)
r	yawing velocity, rad/sec
S	wing area, m^2 (ft^2)
u,v,w	components of resultant velocity V along X, Y, and Z body axes, m/sec (ft/sec)
V	resultant linear velocity, m/sec (ft/sec)
X,Y,Z	body reference axes
α	angle of attack, deg or rad
β	angle of sideslip, deg or rad
ρ	air density, kg/m^3 ($slugs/ft^3$)
$\Delta\theta$	pitch-angle increment, deg
$\Delta\phi$	roll-angle increment, deg
$\Delta\psi$	yaw-angle increment, deg
ω	angular velocity, $2\pi f$, rad/sec

Λ wing sweep angle, deg

A dot over a symbol indicates a derivative with respect to time.

Coefficients and Derivatives

Results are given in terms of coefficients and derivatives as defined in the following tabulations:

Pitch:

$$C_N = \frac{F_N}{q_\infty S} \qquad C_A = \frac{F_A}{q_\infty S} \qquad C_m = \frac{M_Y}{q_\infty S\bar{c}}$$

$$C_{N_q} = \frac{\partial C_N}{\partial \frac{q\bar{c}}{2V}} \qquad C_{A_q} = \frac{\partial C_A}{\partial \frac{q\bar{c}}{2V}} \qquad C_{m_q} = \frac{\partial C_m}{\partial \frac{q\bar{c}}{2V}}$$

$$C_{N_{\dot{\alpha}}} = \frac{\partial C_N}{\partial \frac{\dot{\alpha}\bar{c}}{2V}} \qquad C_{A_{\dot{\alpha}}} = \frac{\partial C_A}{\partial \frac{\dot{\alpha}\bar{c}}{2V}} \qquad C_{m_{\dot{\alpha}}} = \frac{\partial C_m}{\partial \frac{\dot{\alpha}\bar{c}}{2V}}$$

$$C_L = \frac{F_L}{q_\infty S} \qquad C_D = \frac{F_D}{q_\infty S}$$

Roll and yaw:

$$C_l = \frac{M_X}{q_\infty Sb} \qquad C_n = \frac{M_Z}{q_\infty Sb} \qquad C_Y = \frac{F_Y}{q_\infty S}$$

$$C_{l_p} = \frac{\partial C_l}{\partial \frac{pb}{2V}} \qquad C_{n_p} = \frac{\partial C_n}{\partial \frac{pb}{2V}} \qquad C_{Y_p} = \frac{\partial C_Y}{\partial \frac{pb}{2V}}$$

$$C_{l_r} = \frac{\partial C_l}{\partial \frac{rb}{2V}} \qquad C_{n_r} = \frac{\partial C_n}{\partial \frac{rb}{2V}} \qquad C_{Y_r} = \frac{\partial C_Y}{\partial \frac{rb}{2V}}$$

$$C_{l_\beta} = \frac{\partial C_l}{\partial \beta} \qquad C_{n_\beta} = \frac{\partial C_n}{\partial \beta} \qquad C_{Y_\beta} = \frac{\partial C_Y}{\partial \beta}$$

$$C_{l_{\dot{\beta}}} = \frac{\partial C_l}{\partial \frac{\dot{\beta}b}{2V}} \qquad C_{n_{\dot{\beta}}} = \frac{\partial C_n}{\partial \frac{\dot{\beta}b}{2V}} \qquad C_{Y_{\dot{\beta}}} = \frac{\partial C_Y}{\partial \frac{\dot{\beta}b}{2V}}$$

MODEL, APPARATUS, AND TESTING TECHNIQUE

Model and Apparatus

The investigation was conducted with a 1/10-scale model of a variable-sweep fighter configuration having twin vertical tails. A three-view sketch showing the general layout of the model is presented in figure 2 and a photograph of the model is presented in figure 3. Geometric characteristics are given in table I. The model was constructed primarily of molded fiber glass.

The wing sweep angle could be manually varied from 22° (full forward) to 68° (full aft). The wing was provided with full-span leading-edge slats which could be used at the lower sweep angle. A sketch showing details of the slat installation is presented in figure 4.

Preliminary spin-tunnel tests indicated that the developed spin and spin-recovery characteristics of the present configuration could be improved by adding canard surfaces to the fuselage forebody. The present investigation therefore included a study of the effects of these canards on dynamic characteristics at spin attitudes. A sketch showing the location and size of the canards is presented in figure 5.

The tests were made in the 9.1 by 18.3 m (30- by 60-ft) test section of the Langley full-scale tunnel. The test setups for the dynamic pitching, rolling, and yawing tests are illustrated in figure 6. The model was mounted about 3.05 m (10 ft) above the ground board with its wings in a vertical plane. The model was so small in proportion to the dimensions of the tunnel test section that no wind-tunnel jet-boundary or blockage corrections were required. All static force tests were made with a twin-sting support setup (shown in fig. 6(b)) and an internal strain-gage balance.

Testing Technique

An oscillatory motion was imparted to the model by means of a flywheel-driven system of pushrods and bellcranks powered by a 2.2-kW (3-hp) variable-sweep electric motor. The frequency of the oscillation was varied by changing the speed of the electric motor. A precision sine-cosine potentiometer, which generated voltage signals proportional to the sine and cosine of the flywheel rotation angle, was coupled directly to the flywheel shaft and provided electrical signals proportional to the angular displacement of the model. These signals were used in the data-reduction procedure described in detail in reference 2.

TESTS

The investigation was conducted at an airspeed of 20.1 m/sec (66 ft/sec) which corresponds to a Reynolds number of about 0.4×10^6 based on $\bar{c}$. Tests were made for wing sweep angles of 22^o, 35^o, 50^o, and 68^o. A limited number of static force tests were made for $\Lambda = 22^o$, 50^o, and 68^o to aid in the analysis of the dynamic force tests.

The forced-oscillation tests in pitch, roll, and yaw were conducted over an angle-of-attack range from -5^o to 90^o for an angle of sideslip of 0^o. Tests were made for an oscillation amplitude of $\pm 5^o$ and for two oscillation frequencies resulting in values of the reduced-frequency parameter k of 0.152 and 0.305 for the roll and yaw tests and 0.023 and 0.047 for the pitch tests. The effects of the horizontal and vertical tails and the canards were also determined during the study.

The tests were conducted by forcing the model to oscillate at a constant amplitude and frequency at a fixed angle of attack. The return signal from an internally mounted strain-gage balance was then analyzed by an electronic computer which computed dynamic stability derivatives as discussed in reference 2. At least three data points were taken at each angle of attack, and the data presented herein are the average value at each test condition. No significant scatter was noted for these tests.

RESULTS AND DISCUSSION

Static Force Tests

Longitudinal characteristics.- Longitudinal data obtained for the basic configuration are presented in figures 7 and 8. The data presented in figure 7 show the effect of wing sweep angle on the static longitudinal characteristics for $i_t = 0^o$. The results show that the model was statically stable over the entire test angle-of-attack range for all three values of wing sweep. The model at unstalled angles of attack became more stable with increasing wing sweep, as might be expected. Flow-visualization tuft studies indicated that the variable-sweep panels of the wing stalled at about $\alpha = 12^o$ for $\Lambda = 22^o$; however, the data show that the maximum lift coefficient occurred near $\alpha = 30^o$. This result is attributed to the fact that the highly swept fixed-wing glove and broad, flat fuselage of the present configuration produce a great deal of lift at high angles of attack. The significance of this characteristic is that, for $\Lambda = 22^o$, many of the static and dynamic stability derivatives which are usually dependent on wing span loading show marked variations near $\alpha = 12^o$, but other derivatives which are usually dependent on lift coefficient do not exhibit large changes until $\alpha = 30^o$. At wing sweep angles of 50^o and 68^o, there was no evidence of classical stall of the variable-sweep panels of the wing, and maximum lift coefficient occurred near $\alpha = 35^o$.

Presented in figure 8 is the effect of horizontal-tail deflection angle and the effect of removing the horizontal tail for a wing sweep angle of 22°. These data show that the horizontal-tail contribution to static longitudinal stability was reduced markedly in the angle-of-attack range from 20° to 40° and that the tails provided a large nose-down pitching-moment increment near $\alpha = 90^{\circ}$.

As previously mentioned, adding canard surfaces to the fuselage forebody produced considerable improvement in the spin and spin-recovery characteristics of the configuration during spin-tunnel tests. Tests were therefore conducted to determine the effects of the canards (shown in fig. 5) on the static and dynamic aerodynamic characteristics of the model. The effect of the canards on the static longitudinal characteristics is shown in figure 9 for $\Lambda = 22^{\circ}$ and $i_t = 0^{\circ}$. The data show that the canards produced a large reduction in the nose-down pitching moments at angles of attack normally associated with spinning. The reduction in C_m was about equal to that produced by deflection of the horizontal tail to $i_t = -30^{\circ}$. (See fig. 8.) As discussed in reference 3, a reduction in nose-down aerodynamic pitching moment usually tends to reduce the angular rate of a developed spin and enhance the possibility of recovery from the spin. The smaller values of C_m act to reduce the spin rate because of the balance between the inertial and aerodynamic pitching moments acting on an airplane during a spin. These results indicate that the beneficial effect of the canards observed in the spin-tunnel tests may be partly caused by changes in C_m. The canards also improved the dynamic lateral-directional characteristics, as will be discussed in a subsequent section of this paper.

It should be noted that the data of figure 9 show that addition of the canards resulted in longitudinal instability at low angles of attack. It would appear, therefore, that the canards should not be extended until post-stall angles of attack are encountered.

Lateral-directional characteristics.- The static lateral-directional characteristics of the model with the vertical tails on and off were measured at $\beta = \pm 5^{\circ}$ for $\Lambda = 22^{\circ}$, 50°, and 68°. These data are presented in figure 10 as the static lateral-directional stability derivatives C_{Y_β}, C_{n_β}, and C_{l_β}. The data show that the model with the vertical tails on was directionally stable for all wing sweeps at low angles of attack, but as α increased C_{n_β} was markedly reduced; and the model became directionally unstable at about $\alpha = 25^{\circ}$ for all three values of wing sweep. The data obtained with the vertical tails removed show that the contribution of the tails to C_{n_β} was reduced as α increased, and the tails had little effect above $\alpha = 25^{\circ}$. Tuft studies indicated that the loss of vertical-tail effectiveness at high angles of attack was caused by adverse sidewash and loss of dynamic pressure at the location of the vertical tails resulting from flow separation near the juncture of the glove and variable-sweep wing panels.

The data of figure 10 also show that the effective dihedral derivative C_{l_β} became less stable (i.e., less negative) near the angle of attack for maximum lift, and this reduc-

tion in stability increased with wing sweep. For $\Lambda = 68^{\circ}$, C_{l_β} became unstable (positive) at the angle of attack for maximum lift. The combination of directional instability and loss of effective dihedral near maximum lift is conducive to directional divergences which might lead to inadvertent spins. Reference 4 discusses these factors in more detail in relation to directional divergence tendencies of another fighter configuration.

Dynamic Force Tests

Pitching tests.- The effect of wing sweep on the variations of the dynamic longitudinal stability parameters $C_{N_q} + C_{N_{\dot{\alpha}}}$, $C_{A_q} + C_{A_{\dot{\alpha}}}$, and $C_{m_q} + C_{m_{\dot{\alpha}}}$ with angle of attack are presented in figure 11. The data show that the model had stable values of damping in pitch (negative values of $C_{m_q} + C_{m_{\dot{\alpha}}}$) over most of the angle-of-attack range; however, large reductions in damping in pitch occurred near maximum lift ($\alpha = 30^{\circ}$). Additional tests were conducted to determine the effect of the horizontal tails and frequency of the oscillation; these results are presented in figure 12 for each value of wing sweep. The data show that when the horizontal tails were removed, the model exhibited large unstable values of $C_{m_q} + C_{m_{\dot{\alpha}}}$ near the angle of attack for maximum lift for all wing sweeps. These characteristics have been displayed by other airplane configurations in past investigations, and the basic mechanism producing the unstable damping was found to be related to that producing stall flutter. (See, for example, ref. 5.) This instability is caused by aerodynamic hysteresis and associated lag of the flow during oscillatory motions when significant flow separation exists.

The data of figure 12 also show that the horizontal tails provided a stabilizing increment to the damping in pitch over most of the angle-of-attack range and that reduction in the reduced-frequency parameter k from 0.047 to 0.023 caused the model to become more unstable near the angle of attack for maximum lift.

Rolling tests.- The dynamic derivatives measured during the forced-oscillation tests in roll are presented in figures 13 to 15. The effect of wing sweep angle on the dynamic rolling derivatives is shown in figure 13. The model exhibited stable values of damping in roll (negative values of $C_{l_p} + C_{l_{\dot{\beta}}} \sin \alpha$) over the entire test angle-of-attack range for all wing sweeps. At low angles of attack, increasing wing sweep significantly decreased the damping in roll as might be expected. This reduction would be expected inasmuch as roll damping is dependent on lift-curve slope and lower values of lift-curve slope were produced by the reduction in effective aspect ratio. (See fig. 7.) The roll damping for $\Lambda = 22^{\circ}$ decreased rapidly as the outer wing panels stalled near $\alpha = 12^{\circ}$. For higher values of wing sweep, $C_{l_p} + C_{l_{\dot{\beta}}} \sin \alpha$ remained relatively constant up to $\alpha = 20^{\circ}$, then increased up to $\alpha = 30^{\circ}$. This trend in damping from $\alpha = 20^{\circ}$ to $\alpha = 30^{\circ}$ is probably related to the lifting characteristics of the fixed wing glove. Tuft studies showed that as α was increased from 20° to 30°, strong vortices were shed from the glove, and past investigations have shown that this type of flow separation can produce

significant increases in roll damping. (For example, see ref. 6.) As previously discussed, the glove appeared to stall near $\alpha = 30^{\circ}$, and the sudden reduction in roll damping near this angle of attack is a result of this stall. For angles of attack greater than 30°, $C_{l_p} + C_{l_{\dot{\beta}}} \sin \alpha$ decreased markedly.

The results of additional tests conducted to determine the effects of both frequency and the vertical tails are presented in figure 14. The data show that the vertical tails had little effect on the dynamic rolling derivatives. For low values of wing sweep ($\Lambda = 22^{\circ}$ and 35°), variation of k from 0.305 to 0.152 (lower frequency of oscillation) had no significant effect on the damping in roll. For $\Lambda = 68^{\circ}$, large effects of frequency on $C_{l_p} + C_{l_{\dot{\beta}}} \sin \alpha$ were measured above $\alpha = 20^{\circ}$. These effects are believed to be caused by variations in $C_{l_{\dot{\beta}}}$ at high angles of attack. The dependence of the $\dot{\beta}$ derivatives on frequency at high angles of attack has been documented by past investigations (see ref. 7, for example) and is attributed to lag of flow separation and attachment for highly swept wings.

Additional tests were conducted in an attempt to delay the onset of loss of roll damping for $\Lambda = 22^{\circ}$. These tests consisted of adding the leading-edge slats shown in figure 4 to the variable-sweep panels of the wing in order to delay stall. The results of these tests, presented in figure 15, show that the slats significantly improved the damping in roll near $\alpha = 12^{\circ}$. This improvement was caused by the fact that adding the slats delayed stall of the variable-sweep panels from 12° for the basic wing to about 20° for the slatted wing.

Yawing tests.- The results of the dynamic yawing tests are presented in figures 16 and 17. The effect of wing sweep on the dynamic yawing derivatives is shown in figure 16. The data show little effect of wing sweep on the derivatives for the conditions investigated. The model exhibited stable values of damping in yaw $\left(\text{negative values of } C_{n_r} - C_{n_{\dot{\beta}}} \cos \alpha\right)$ for angles of attack up to about 45°. The damping in yaw was relatively low and actually unstable for some portions of the angle-of-attack range from 50° to 90°, and these unstable values may produce autorotation or a tendency to spin. Similar unstable values of damping in yaw have previously been encountered for other fighter configurations, and the significance of these unstable yaw damping values is discussed in detail in references 8 and 9. The rolling-moment-due-to-yaw parameter $\left(C_{l_r} - C_{l_{\dot{\beta}}} \cos \alpha\right)$ attained a maximum value near $\alpha = 30^{\circ}$ for all values of wing sweep.

The effects of frequency and the vertical tails on the dynamic yawing derivatives are presented in figure 17. The vertical tails produced a stabilizing increment to the damping in yaw for angles of attack below about 35°, but for higher angles of attack, the tails had no appreciable effect. This result correlates well with the reduced vertical-tail effectiveness shown by the static lateral-directional data in figure 10. At $\Lambda = 50^{\circ}$ and 68°, increasing the frequency reduced the yawing-moment parameter near the angle of attack for maximum lift; these effects are caused by factors similar to the hysteresis and lag effects mentioned for the rolling derivatives and are discussed in detail in reference 7.

The most significant result of the dynamic force tests with regard to aerodynamic characteristics associated with spins was the existence of unstable values of the damping-in-yaw parameter $C_{n_r} - C_{n_{\dot{\beta}}} \cos \alpha$ at high angles of attack (figs. 16 and 17). An indication as to the airframe components producing the propelling moments can be obtained by the analysis of the relationship of the yawing moment and side force acting on the airplane during the spin. Figure 18 shows a plan view of an airplane during a right spin. If the fuselage forebody is producing the propelling moments due to yaw rate, a side force of the same sign as the yawing moment will exist. If the tail components are producing the propelling moments, the side force will have an opposite sign. The data of figure 17 show that positive (side force to the right) values of $C_{Y_r} - C_{Y_{\dot{\beta}}} \cos \alpha$ accompanied the positive values of yawing moment due to yaw rate. Based on this analysis, the nose of the configuration was primarily responsible for the propelling moments.

Effect of canards.- The results of tests conducted with the canards shown in figure 5 on the fuselage forebody are presented in figure 19. The data show that the canards eliminated the unstable damping in yaw at high angles of attack. It therefore appears that the beneficial effects of canards noted in the spin-tunnel tests may be attributed to the increased damping in yaw shown in figure 19 and to the reduction in C_m shown in figure 9.

Nonlinear Characteristics

Past wind-tunnel investigations have shown that the variation of C_n with rate of rotation may be extremely nonlinear. Since forced-oscillation tests are limited to relatively low rotational rates, additional methods must be used to determine whether significant aerodynamic nonlinearities exist. Some of this information can be obtained from an analysis of static wind-tunnel force tests.

Shown in figure 20 is the sideslip angle generated at the front of the airplane during a right spin. The sketch on the left-hand side of the figure shows the plan view of the airplane during a right spin with zero bank angle. The arrows along the fuselage nose indicate the relative magnitude and sense of the linear sideward velocities along the fuselage due to the spinning rotation. The sketch on the right-hand side of the figure illustrates the sideslip angle at a typical nose location due to the spin rotation. As can be seen, the airplane rate of descent and the sideward velocity at the nose of the airplane combine vectorially to produce a positive sideslip angle β at the nose; the relative magnitude of β increases with increasing spin rate. Because of the dependence of β on yaw rate, when the variation of C_n with β is found to be nonlinear from the static data, this is an indication of possible nonlinear dynamic aerodynamic characteristics (variation of C_n with $rb/2V$) if the spin rates are high enough. The data of figure 21 show that the variation of

C_n with β was quite nonlinear for the basic configuration whereas the variation was almost linear for the configuration with canards. Based on the foregoing analysis and test results, the variation of C_n with rate of rotation in a spin would be expected to be nonlinear for the basic configuration and less nonlinear for the configuration with canards. In order to verify this theory, a limited number of tests were made in the Langley high-speed 7- by 10-foot tunnel on a special test apparatus which produced continuous yaw rate A model of the present configuration was subjected to continuous 360° rotation in yaw at $\alpha = 85^{\circ}$ and the resulting yawing-moment characteristics are presented in figure 22. Data are shown for the basic configuration for $\Lambda = 22^{\circ}$ and $i_t = 0^{\circ}$ and for the modified configuration with canards. The model was tested for both right and left yaw rates. The data show that the variation of C_n with $rb/2V$ was very nonlinear for the basic configuration. In particular, propelling values of C_n were produced by small values of $rb/2V$, and the propelling moments decreased as rate of rotation increased. Potential equilibrium conditions ($C_n = 0$) are indicated near $rb/2V = \pm 0.3$; these equilibrium conditions were also indicated by spin-tunnel tests. These trends correlate well with the conclusions drawn from the static data of figure 21. When canards were added, the variation of yawing-moment characteristics with rate of rotation became relatively linear, and large increases in the damping moment were obtained near $rb/2V = 0.3$. These trends also agree well with the data of figure 21.

The nonlinear characteristic shown by the data for the basic configuration should be included in a realistic mathematical representation of the aerodynamic characteristics of the present configuration during spins.

CONCLUSIONS

As a result of an analysis of the dynamic stability derivatives of a variable-sweep fighter configuration over an angle-of-attack range from -5° to 90° at a Reynolds number of 0.4×10^6, the following conclusions are noted:

1. The model exhibited stable values of damping in pitch, roll, and yaw over the angle-of-attack range below stall.

2. Large reductions in damping in pitch occurred near maximum lift.

3. Unstable values of damping in yaw were produced by the fuselage forebody at high angles of attack.

4. The unstable values of damping in yaw were eliminated by the addition of canards to the fuselage forebody.

5. The variation of yawing moment with rate of yaw is nonlinear for the present configuration at the angles of attack typically obtained during flat spins, and this nonlinearity was indicated by static and dynamic data.

Langley Research Center,
National Aeronautics and Space Administration,
Hampton, Va., August 3, 1972.

REFERENCES

1. Mechtly, E. A.: The International System of Units – Physical Constants and Conversion Factors (Revised). NASA SP-7012, 1969.

2. Chambers, Joseph R.; and Grafton, Sue B.: Static and Dynamic Longitudinal Stability Derivatives of a Powered 1/9-Scale Model of a Tilt-Wing V/STOL Transport. NASA TN D-3591, 1966.

3. Neihouse, Anshal I.; Klinar, Walter J.; and Scher, Stanley H.: Status of Spin Research for Recent Airplane Designs. NASA TR R-57, 1960. (Supersedes NACA RM L57F12.)

4. Chambers, Joseph R.; and Anglin, Ernie L.: Analysis of Lateral-Directional Stability Characteristics of a Twin-Jet Fighter Airplane at High Angles of Attack. NASA TN D-5361, 1969.

5. Halfman, Robert L.; Johnson, H. C.; and Haley, S. M.: Evaluation of High-Angle-of-Attack Aerodynamic-Derivative Data and Stall-Flutter Prediction Techniques. NACA TN 2533, 1951.

6. Boyden, Richmond P.: Effects of Leading-Edge Vortex Flow on the Roll Damping of Slender Wings. J. Aircraft, vol. 8, no. 7, July 1971, pp. 543-547.

7. Campbell, John P.; Johnson, Joseph L., Jr.; and Hewes, Donald E.: Low-Speed Study of the Effect of Frequency on the Stability Derivatives of Wings Oscillating in Yaw With Particular Reference to High Angle-of-Attack Conditions. NACA RM L55H05, 1955.

8. Chambers, Joseph R.; Anglin, Ernie L.; and Bowman, James S., Jr.: Effects of a Pointed Nose on Spin Characteristics of a Fighter Airplane Model Including Correlation With Theoretical Calculations. NASA TN D-5921, 1970.

9. Chambers, Joseph R.; Bowman, James S., Jr.; and Anglin, Ernie L.: Analysis of the Flat-Spin Characteristics of a Twin-Jet Swept-Wing Fighter Airplane. NASA TN D-5409, 1969.

TABLE I.- GEOMETRIC CHARACTERISTICS OF THE MODEL

Wing:		
Span (based on $\Lambda = 20^{o}$), m (ft)	1.95	(6.41)
Reference area (excluding glove, extended to plane of symmetry), m^2 (ft^2)	0.53	(5.65)
Root chord, cm (in.)	43	(16.72)
Tip chord, cm (in.)	11	(4.43)
Mean aerodynamic chord, cm (in.)	30	(11.76)
Aspect ratio	7.28	
Taper ratio	0.27	
Dihedral, deg	-1.14	
Spoilers -		
Area (one side), m^2 (ft^2)	0.0139	(0.15)
Horizontal tail:		
Area (total exposed), m^2 (ft^2)	0.13	(1.40)
Span, m (ft)	1.03	(3.38)
Aspect ratio	2.56	
Taper ratio	0.21	
Dihedral, deg	-3.5	
Vertical tail:		
Area (each), m^2 (ft^2)	0.05	(0.59)
Span, cm (in.)	26	(10.20)
Aspect ratio (each)	2.45	
Taper ratio	0.36	
Toe-in angle, deg	1	
Cant angle, deg	5	
Rudder -		
Area (each), m^2 (ft^2)	0.0149	(0.16)
Hinge-line location, percent surface chord	70.00	
Ventral fins:		
Area (each), m^2 (ft^2)	0.0084	(0.09)

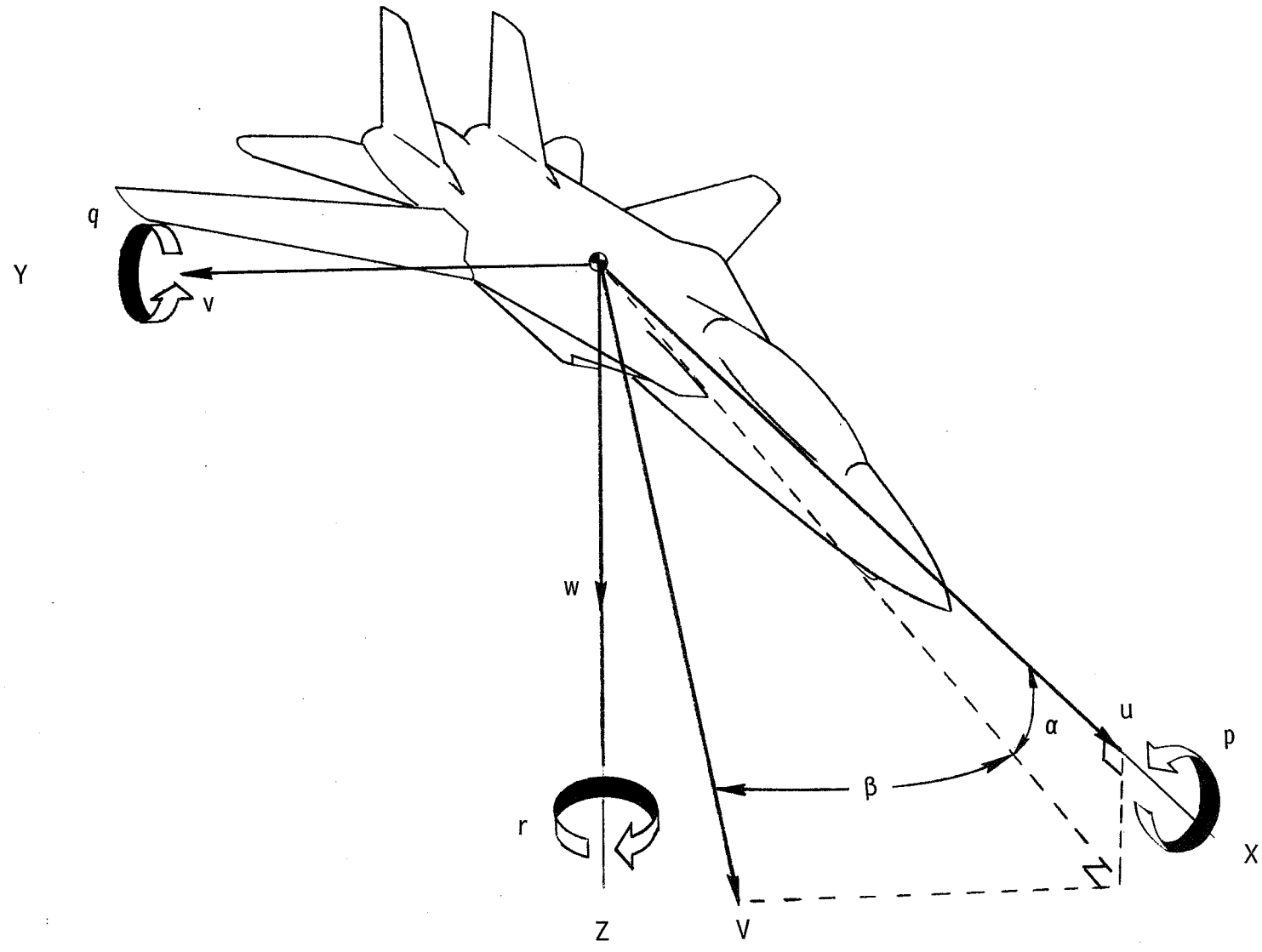

Figure 1.- The body system of axes.

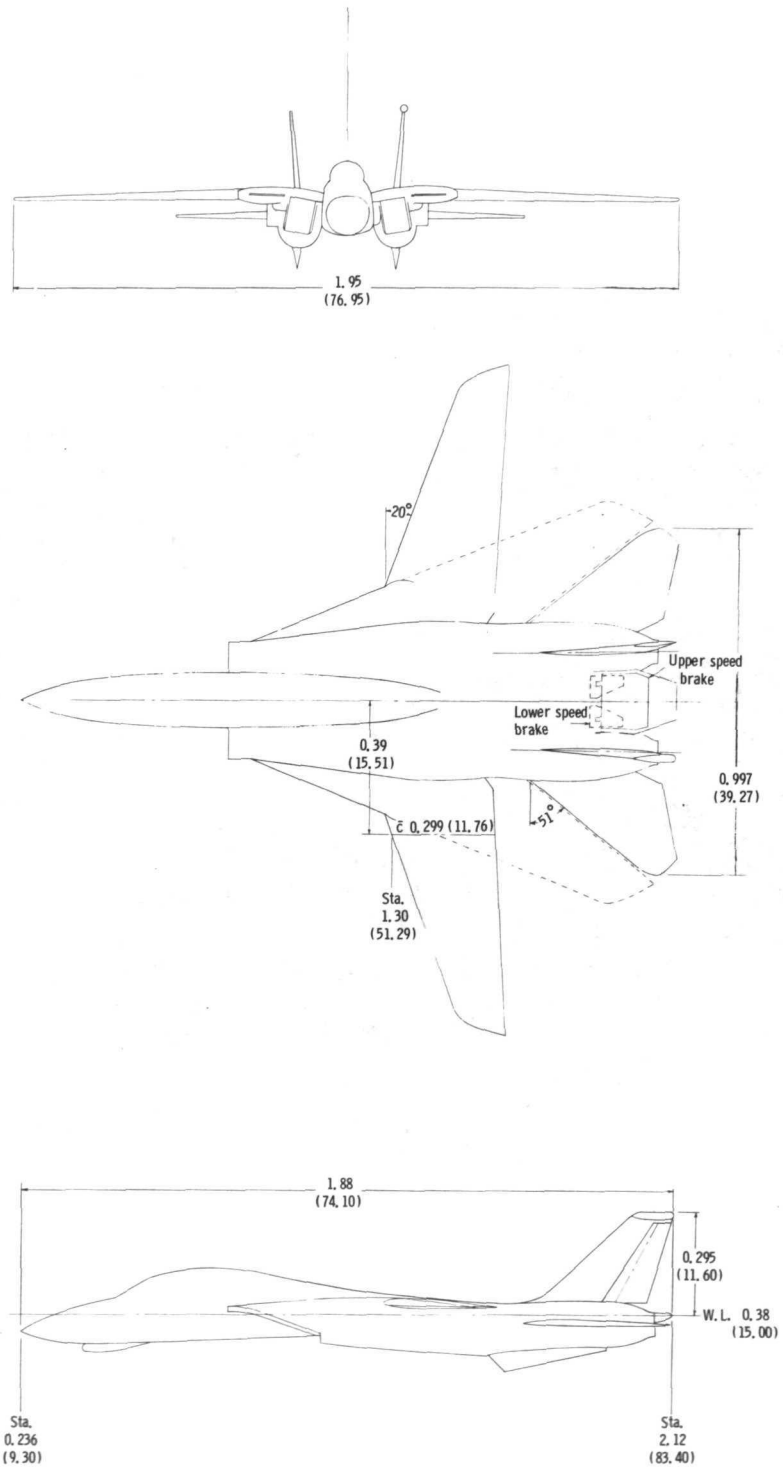

Figure 2.- Sketches of model used in investigation. All linear dimensions are in meters (inches).

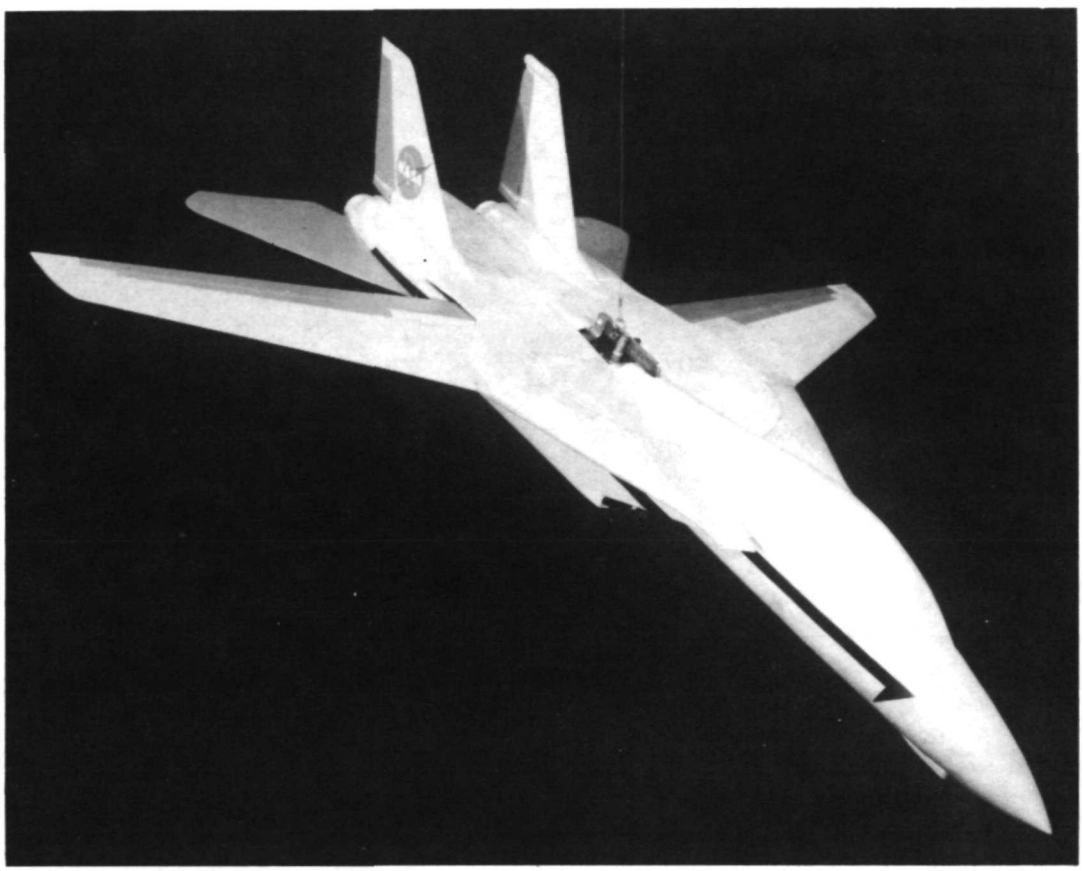

L-70-8838

Figure 3.- Photograph of model.

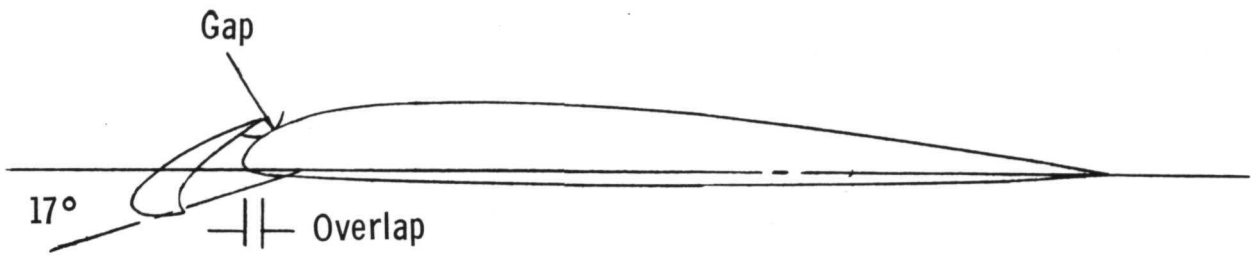

Wing leading-edge slat

Span station, m (in)	Overlap, percent c	Gap, percent c
0.32 (12.88)	1.25	2.0
.91 (35.83)	.50	2.0

Figure 4.- Leading-edge slat details.

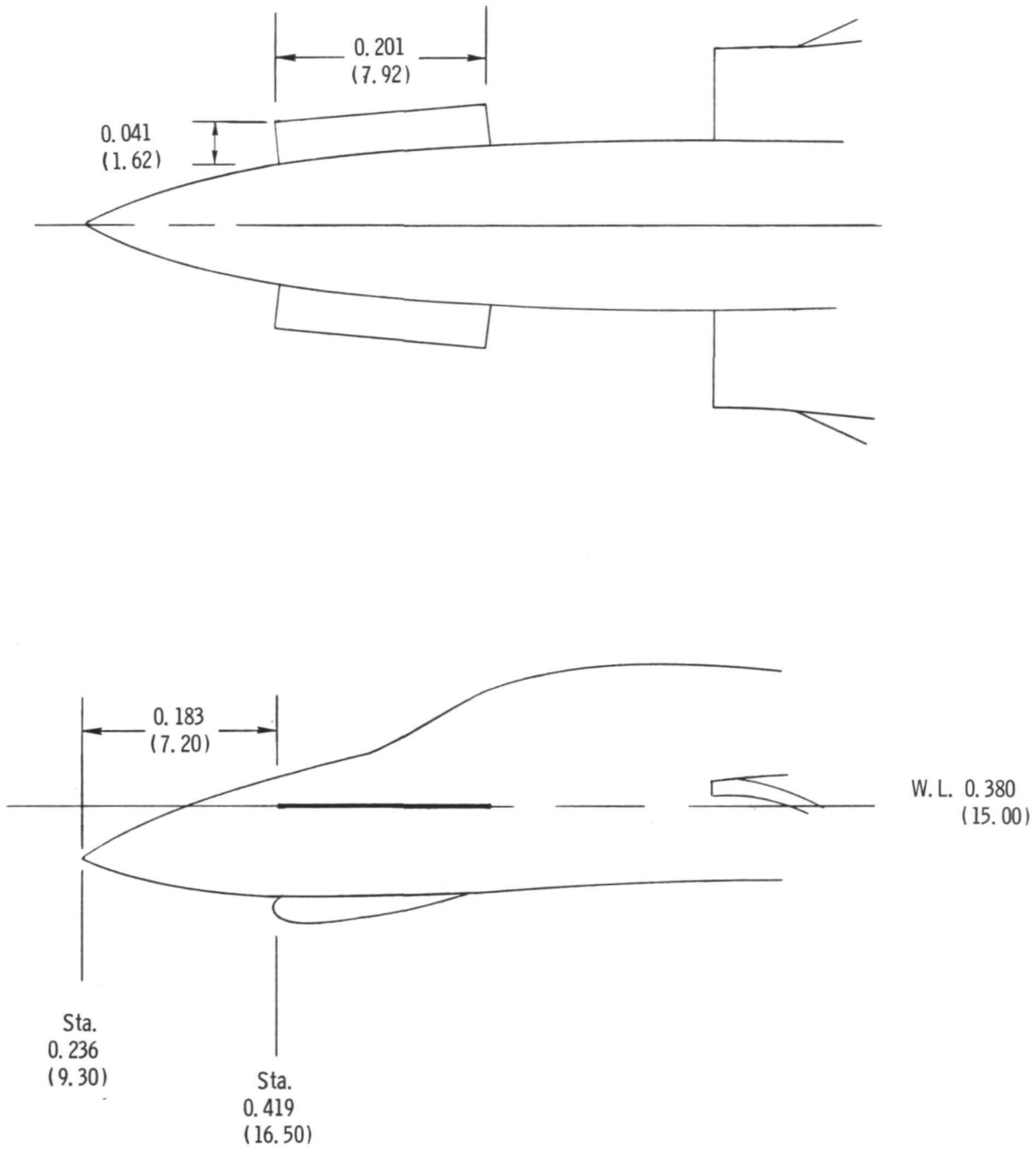

Figure 5.- Sketch of canards used in investigation. All linear dimensions are in meters (inches).

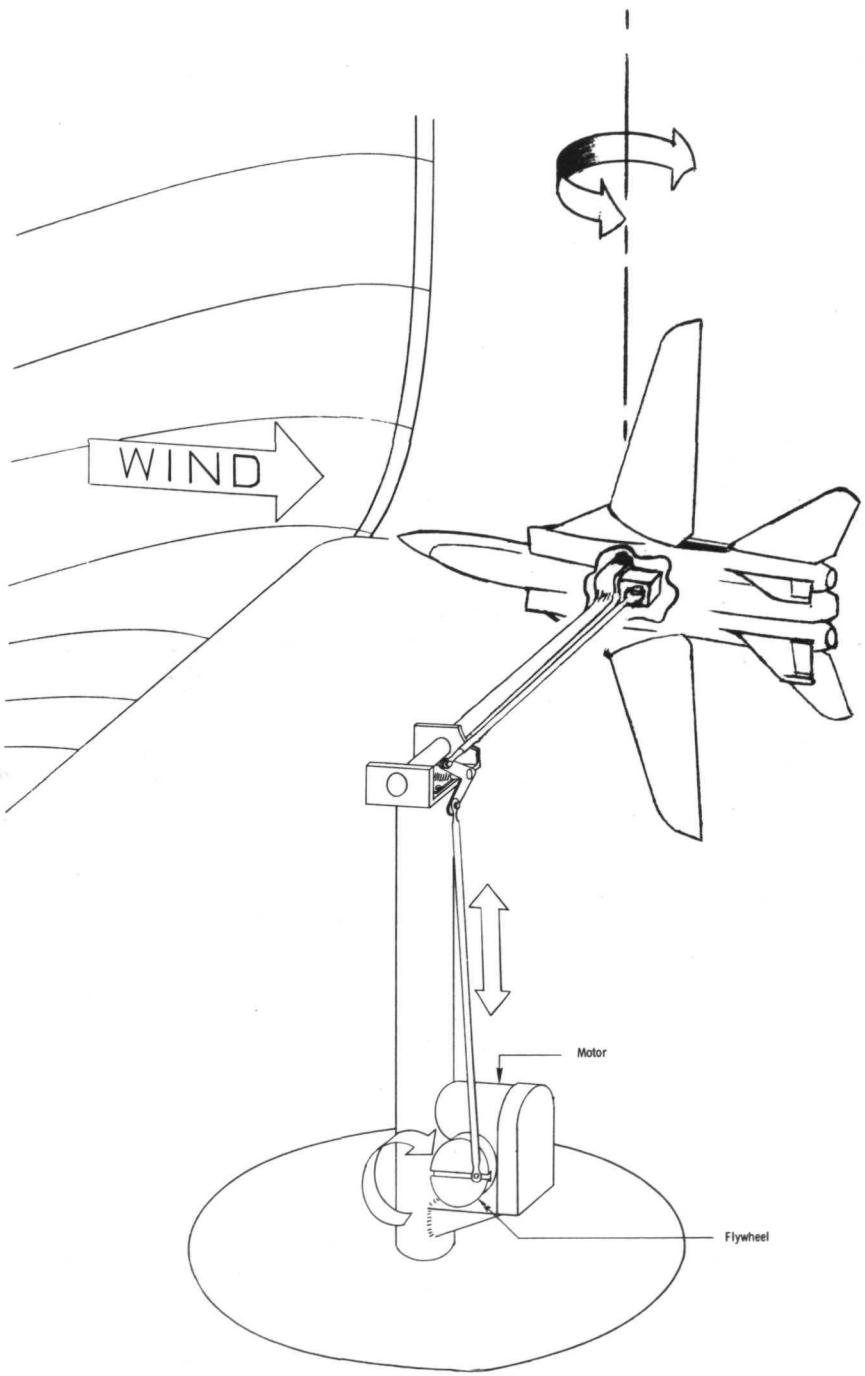

(a) Pitching setup.

Figure 6.- Sketches of forced-oscillation test setups.

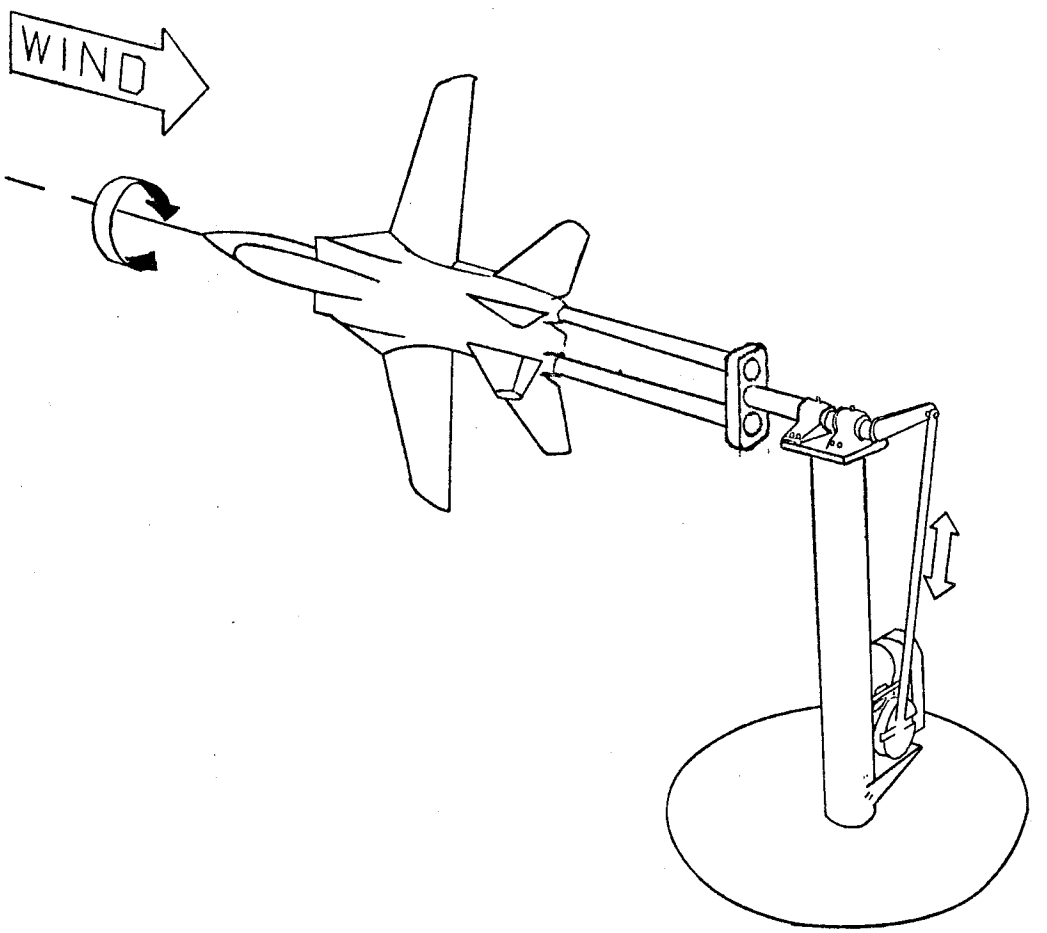

(b) Rolling setup.

Figure 6.- Continued.

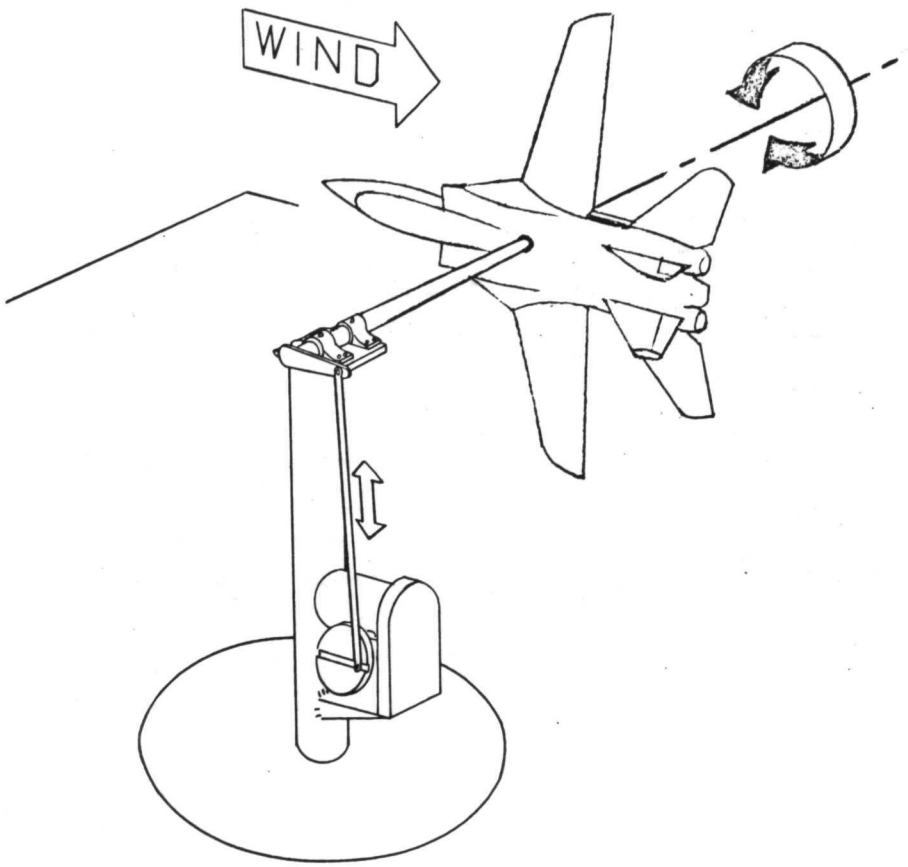

(c) Yawing setup.

Figure 6.- Concluded.

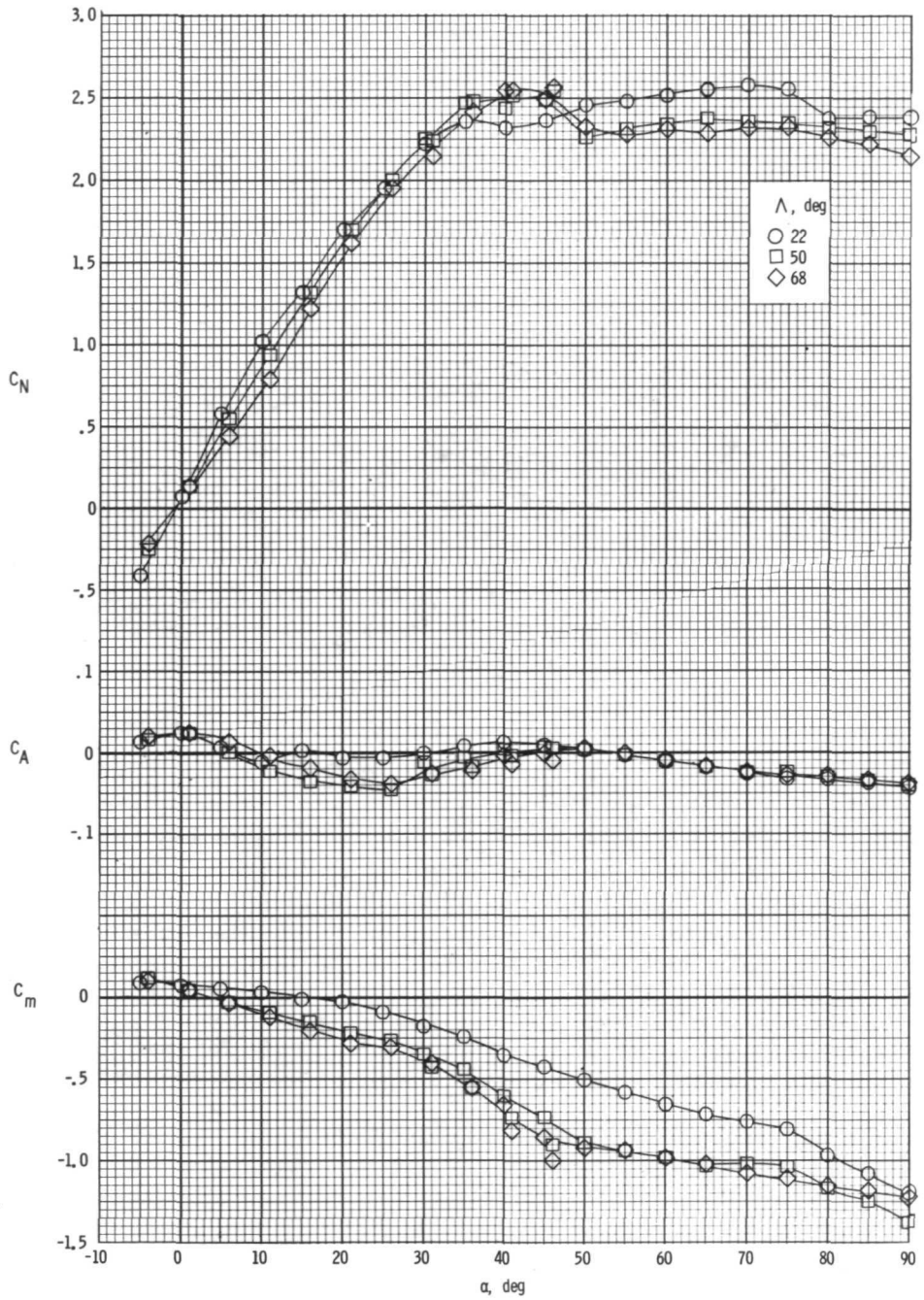

Figure 7.- Effect of wing sweep on static longitudinal characteristics. $i_t = 0^o$.

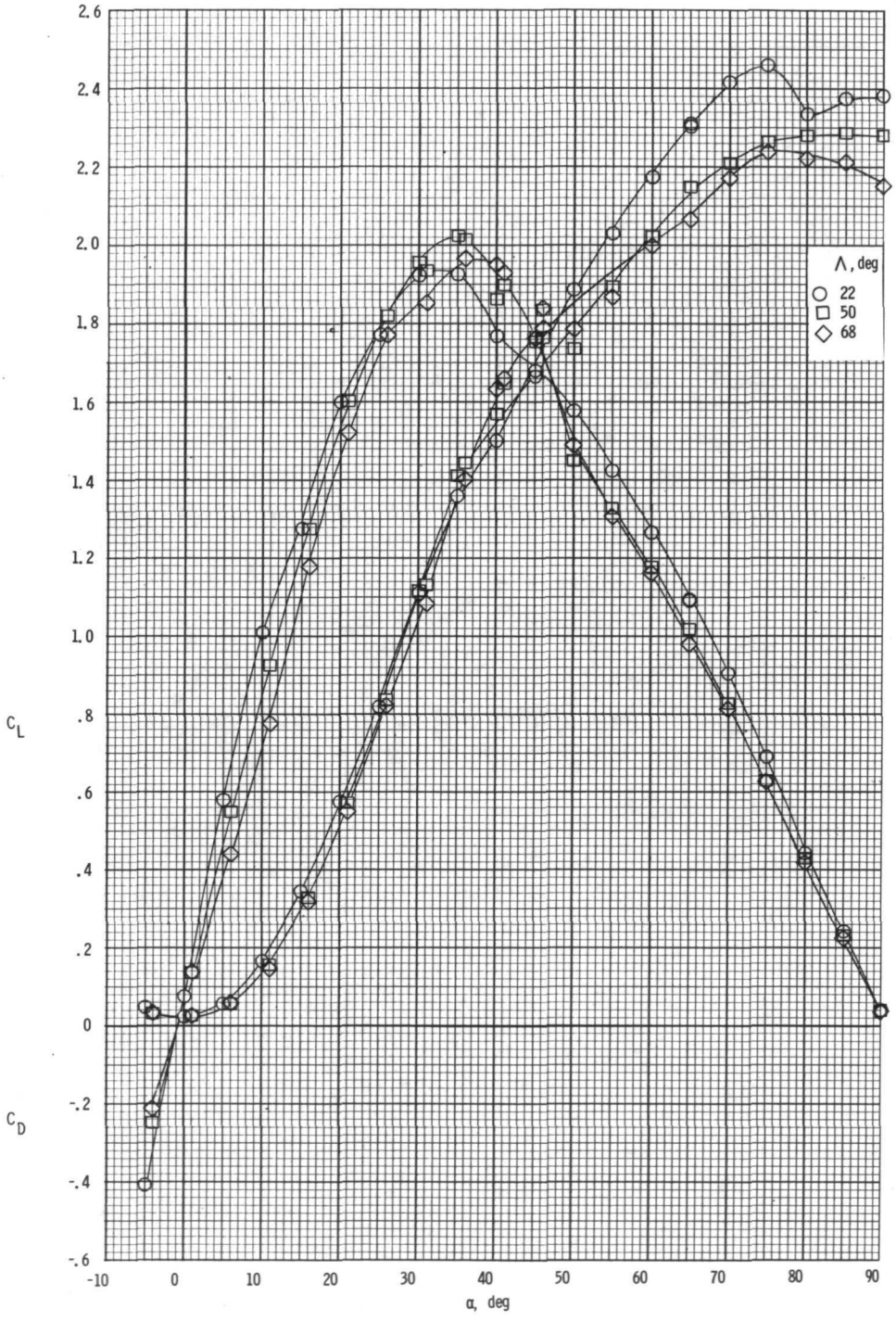

Figure 7.- Concluded.

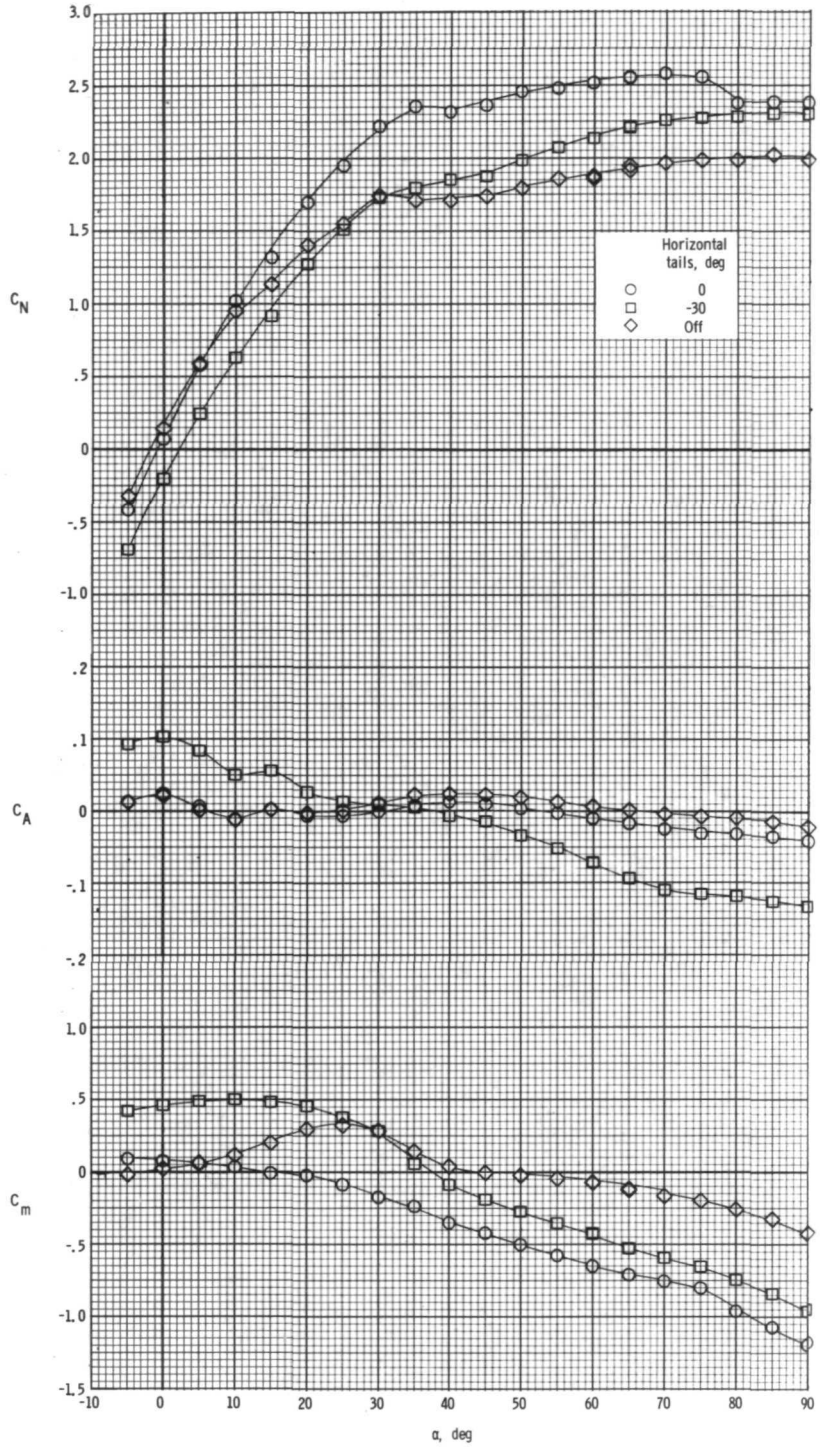

Figure 8.- Effect of horizontal-tail deflection on static longitudinal characteristics. $\Lambda = 22^{o}$.

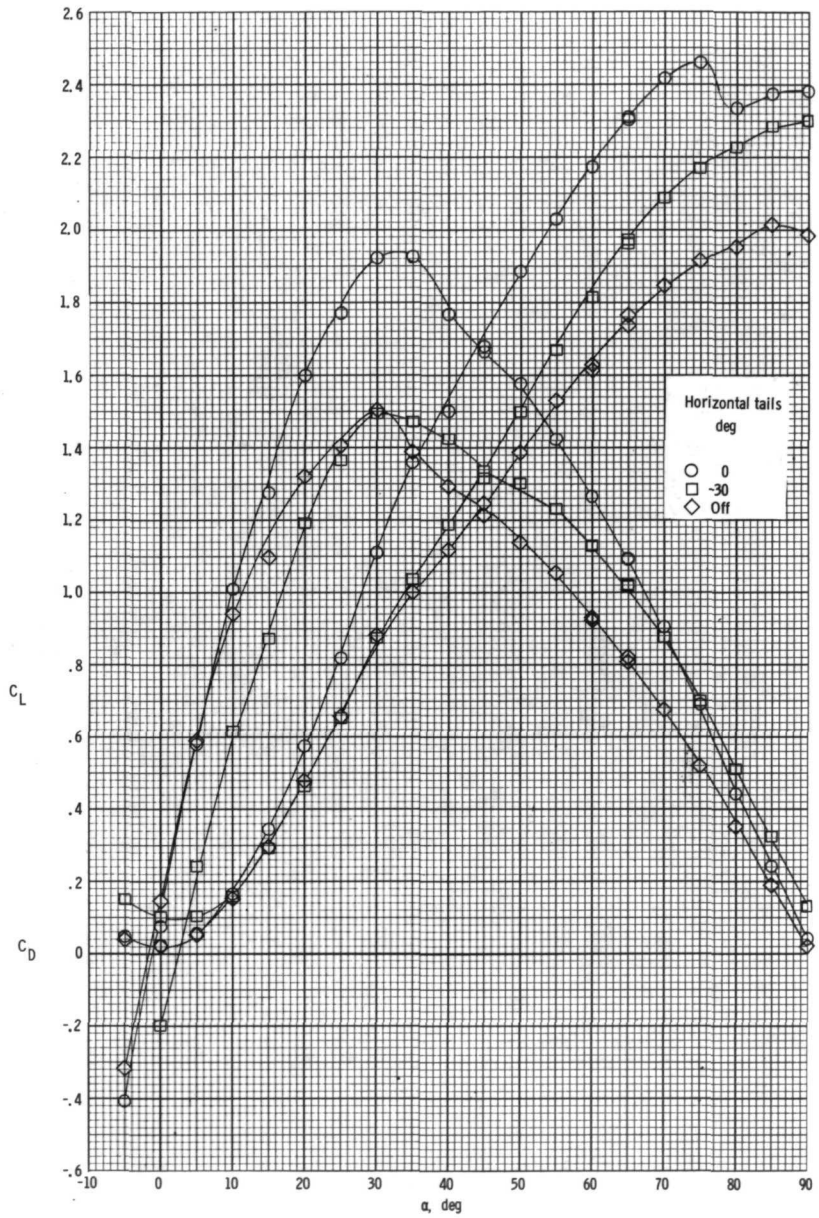

Figure 8.- Concluded.

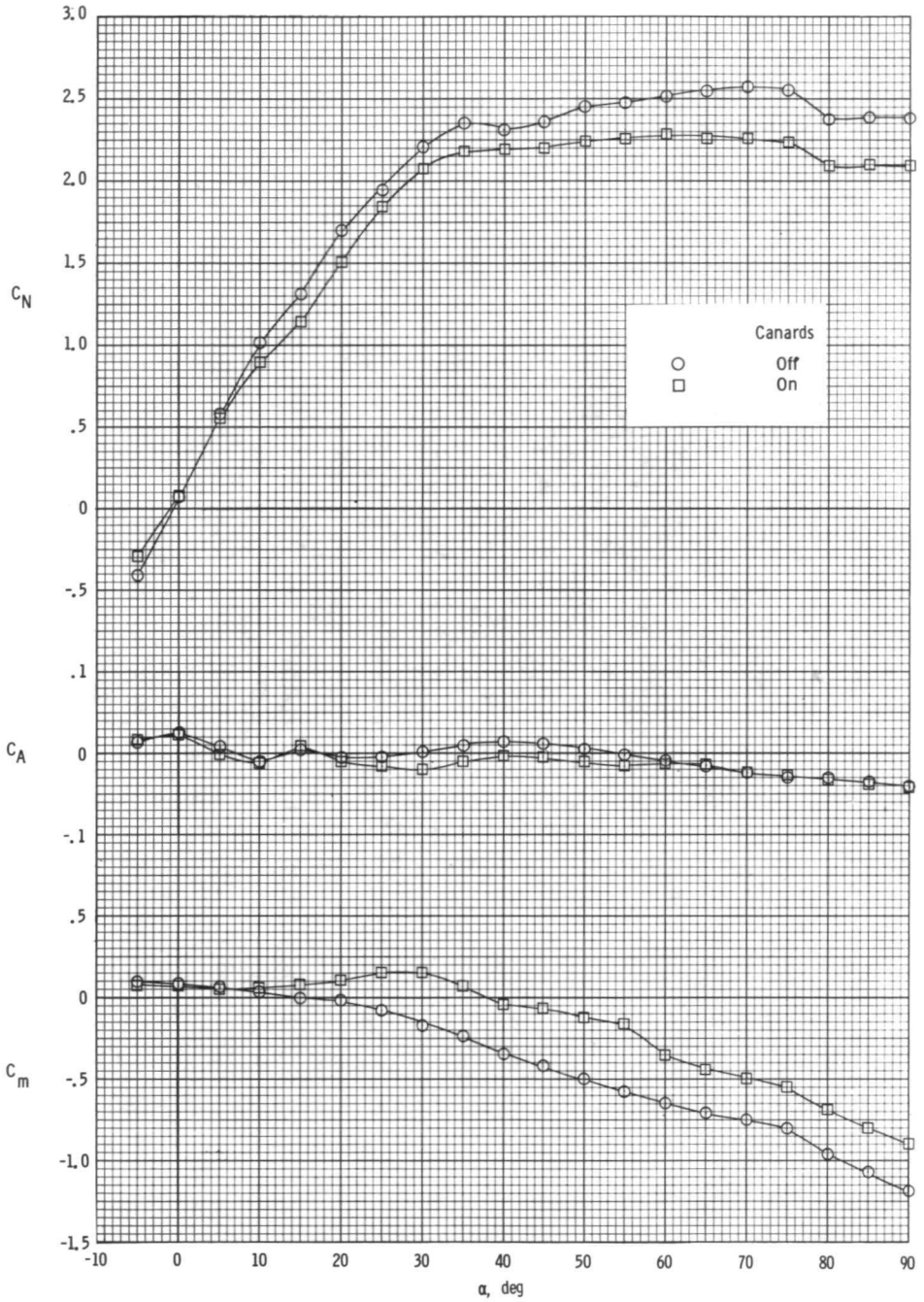

Figure 9.- Effect of canards on static longitudinal characteristics. $\Lambda = 22^{o}$; $i_t = 0^{o}$.

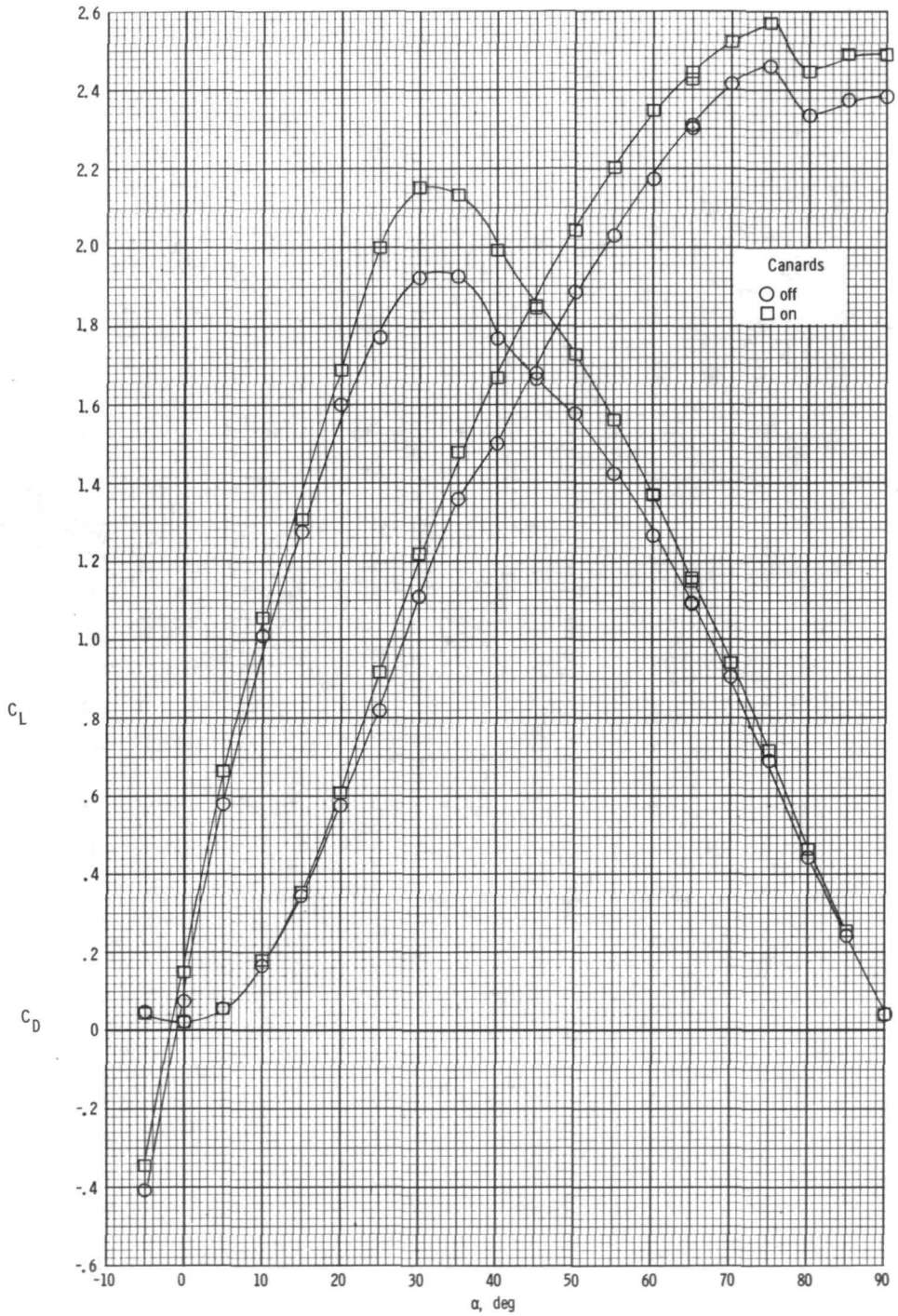

Figure 9.- Concluded.

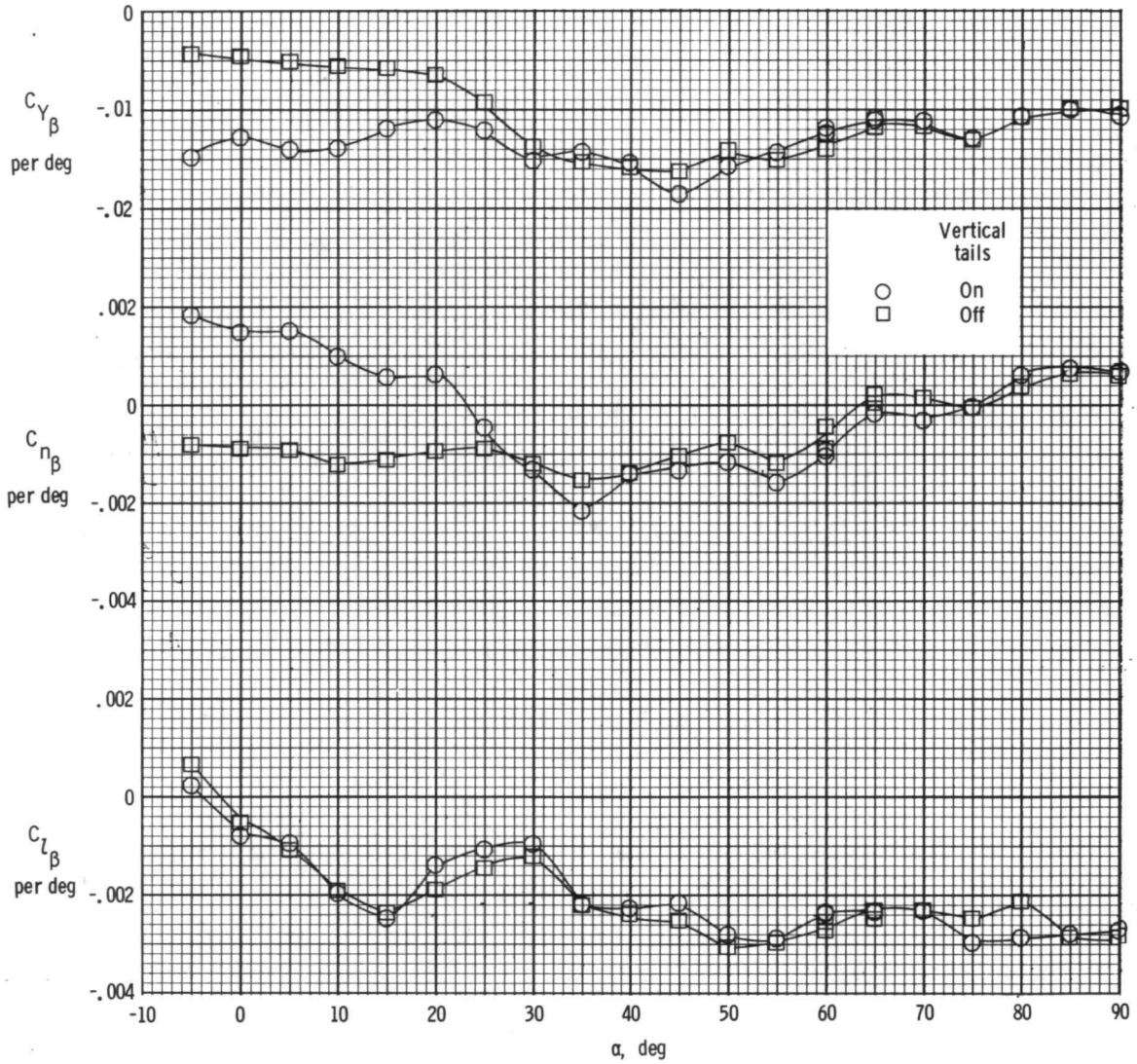

(a) $\Lambda = 22^{o}$.

Figure 10.- Static lateral-directional stability derivatives of model. $i_t = 0^{o}$; $\beta = \pm 5^{o}$.

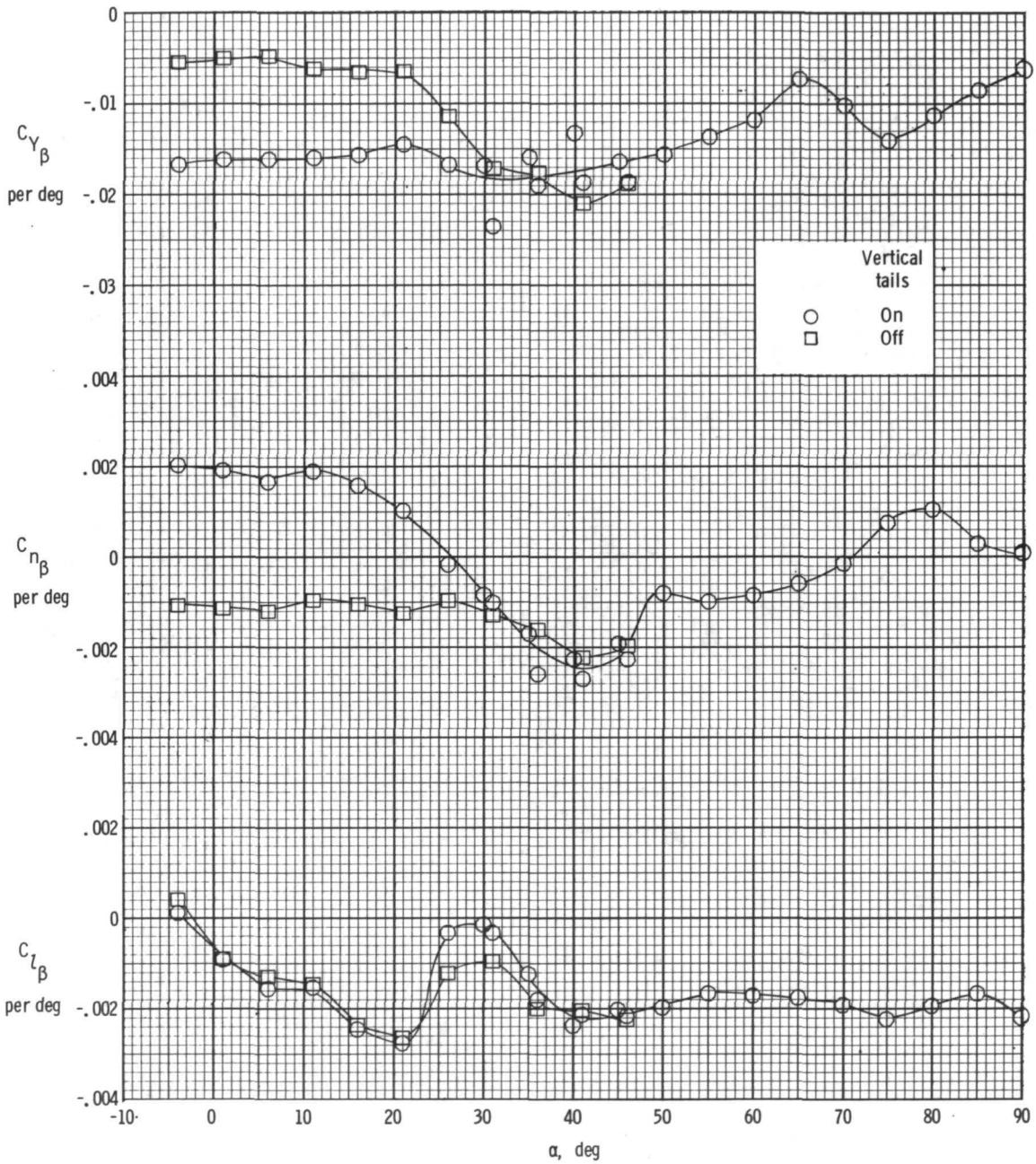

(b) $\Lambda = 50^{o}$.

Figure 10.- Continued.

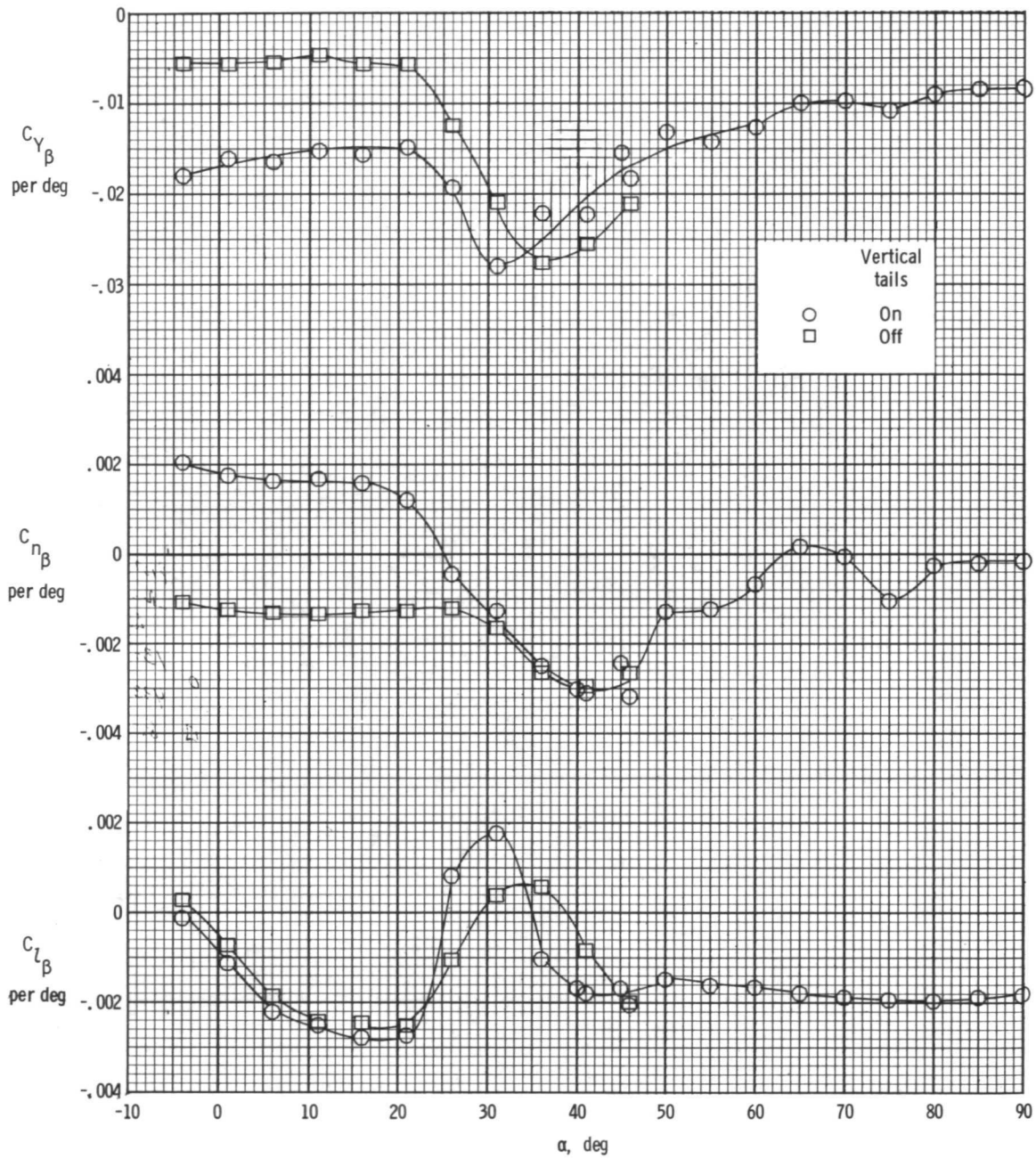

(c) $\Lambda = 68^{o}$.

Figure 10.- Concluded.

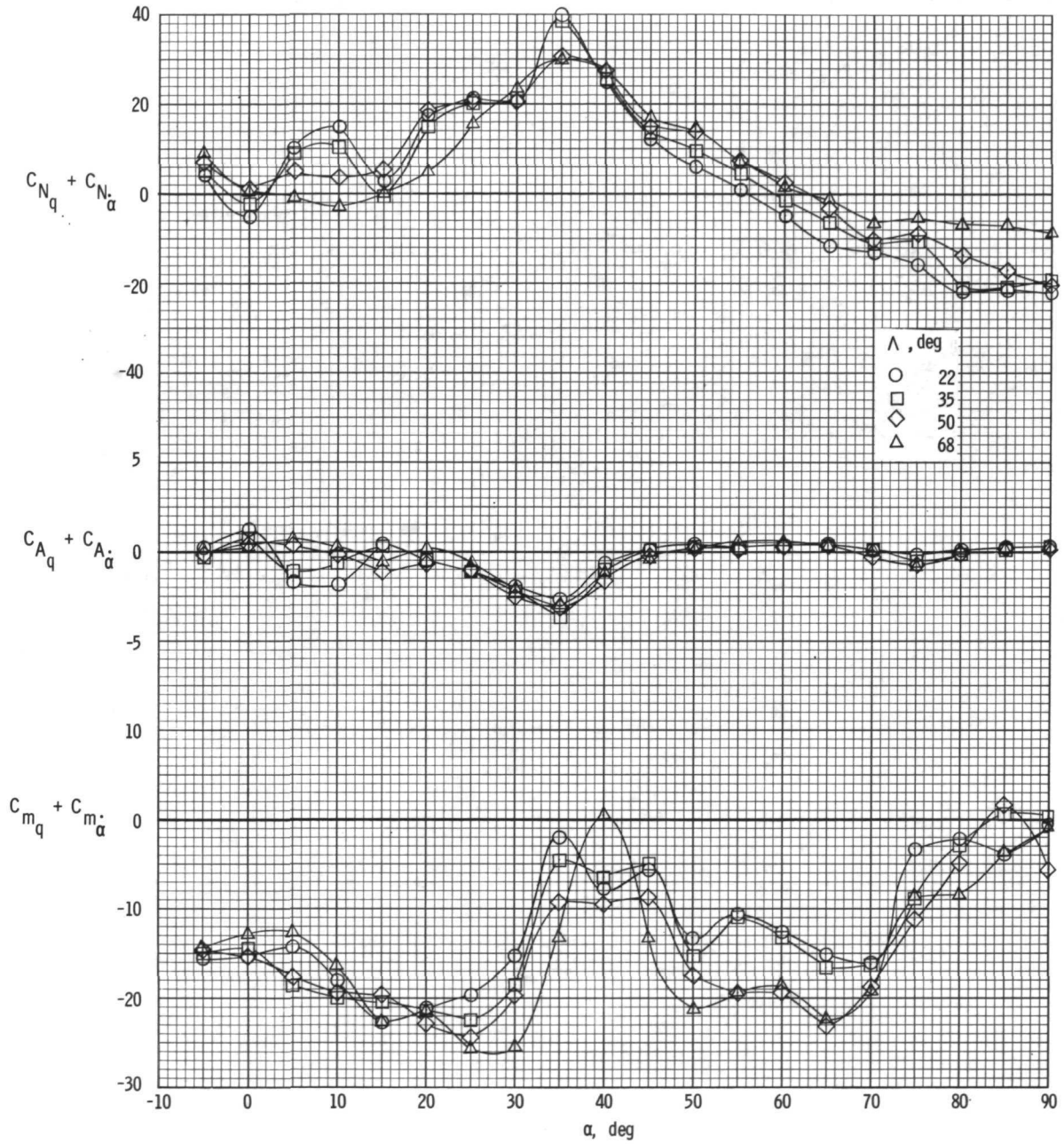

Figure 11.- Effect of wing sweep on the dynamic pitching derivatives. $\Delta\theta = \pm 5^{o}$; $i_t = 0^{o}$; $k = 0.047$.

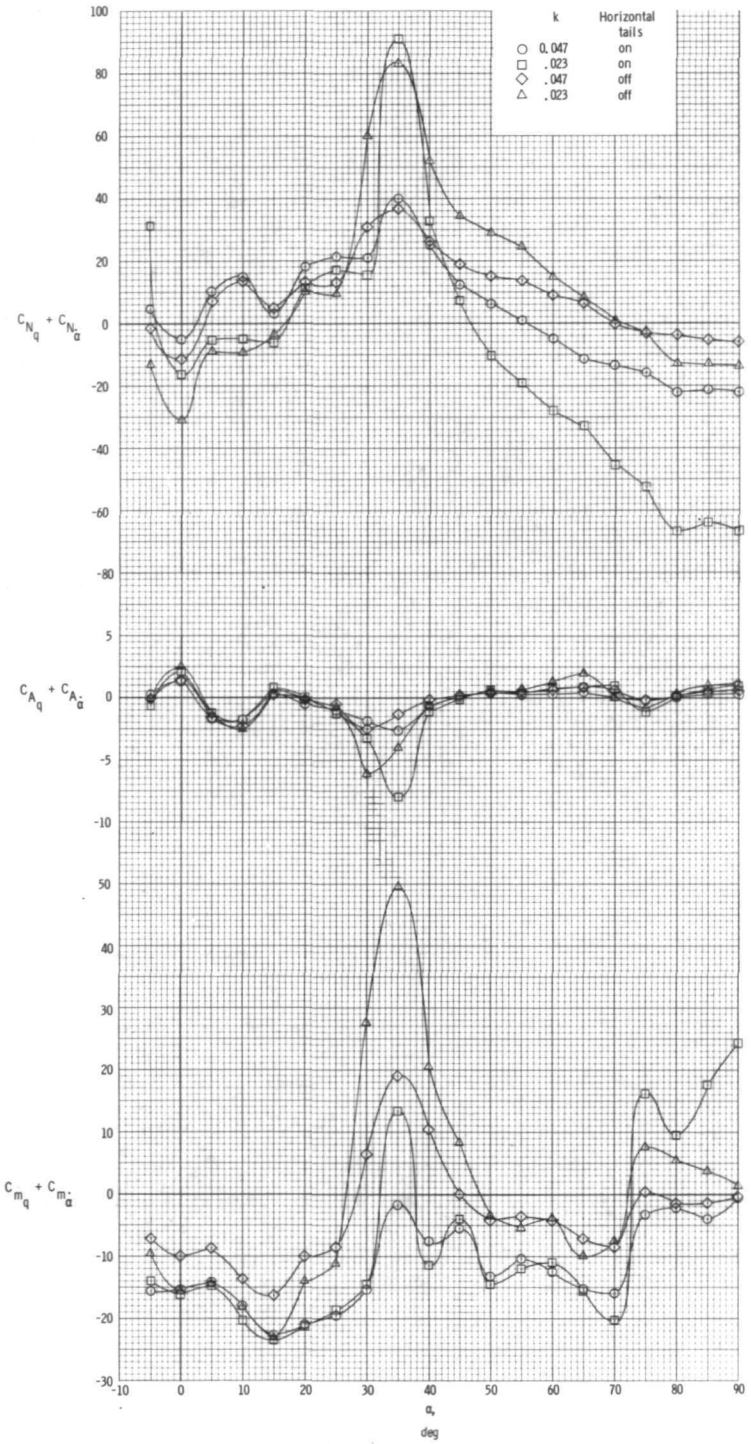

(a) $\Lambda = 22^{\circ}$.

Figure 12.- Effects of frequency and horizontal tails on the dynamic pitching derivatives. $\Delta\theta = \pm 5^{\circ}$.

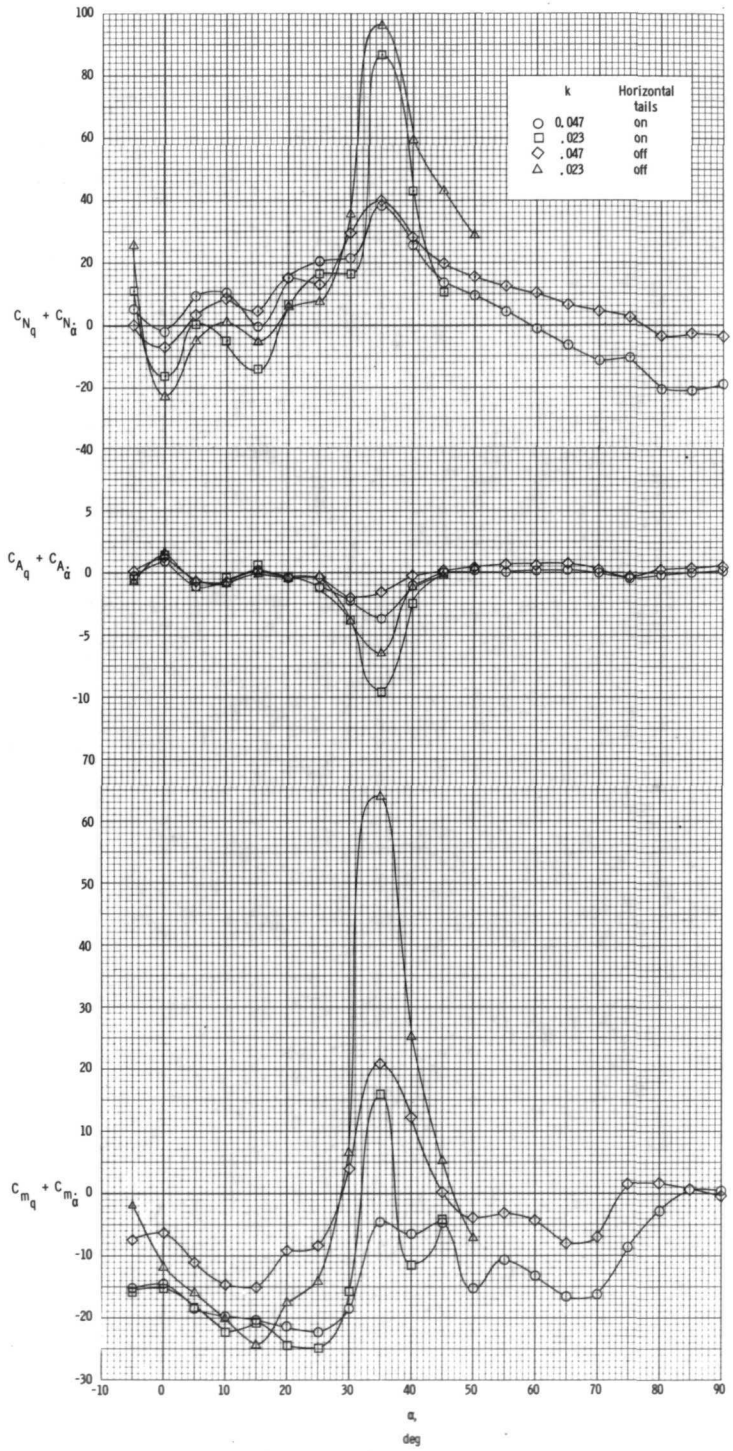

(b) $\Lambda = 35^{\circ}$.

Figure 12.- Continued.

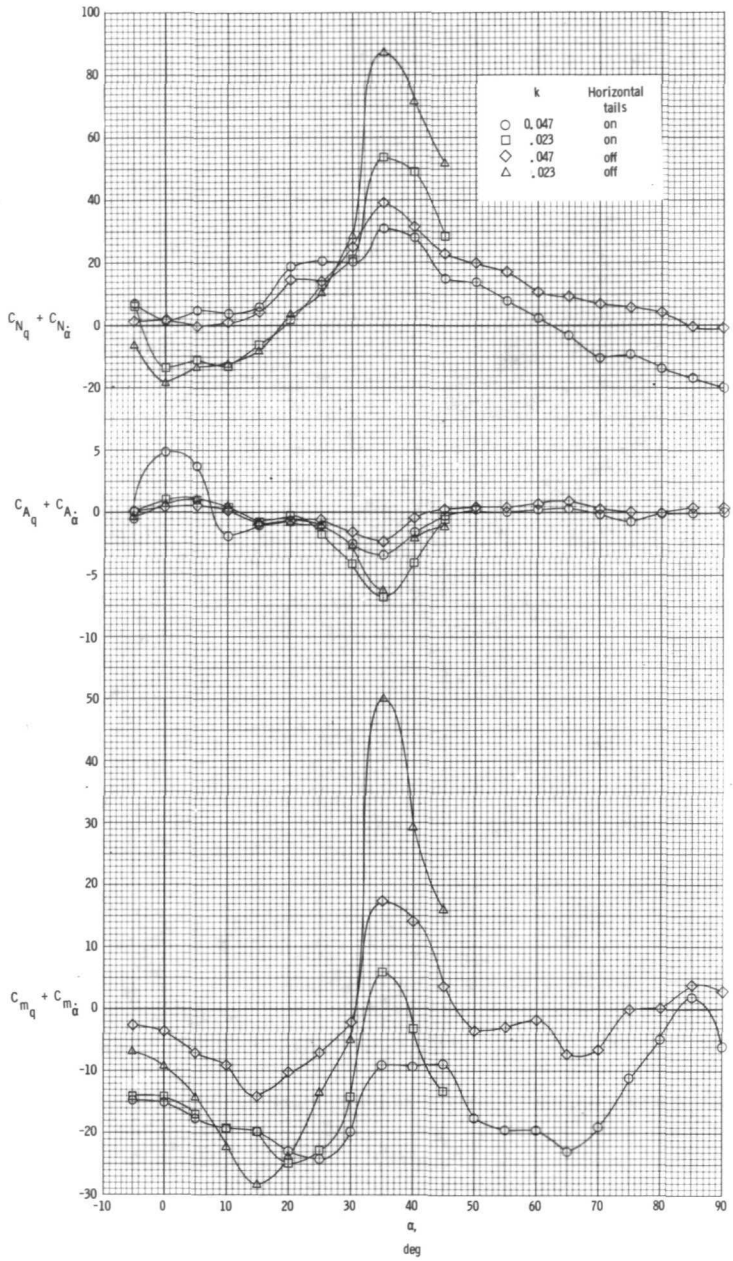

(c) $\Lambda = 50^{o}$.

Figure 12.- Continued.

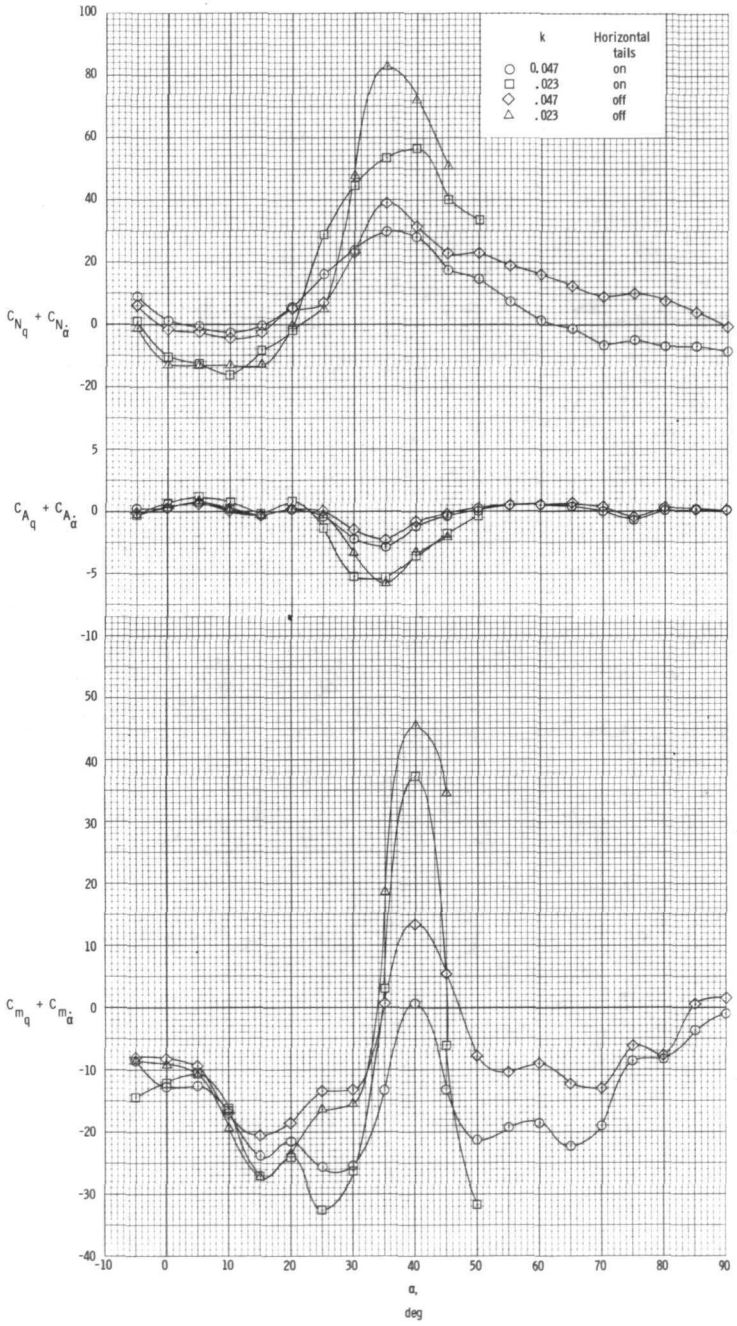

(d) $\Lambda = 68^{\circ}$.

Figure 12.- Concluded.

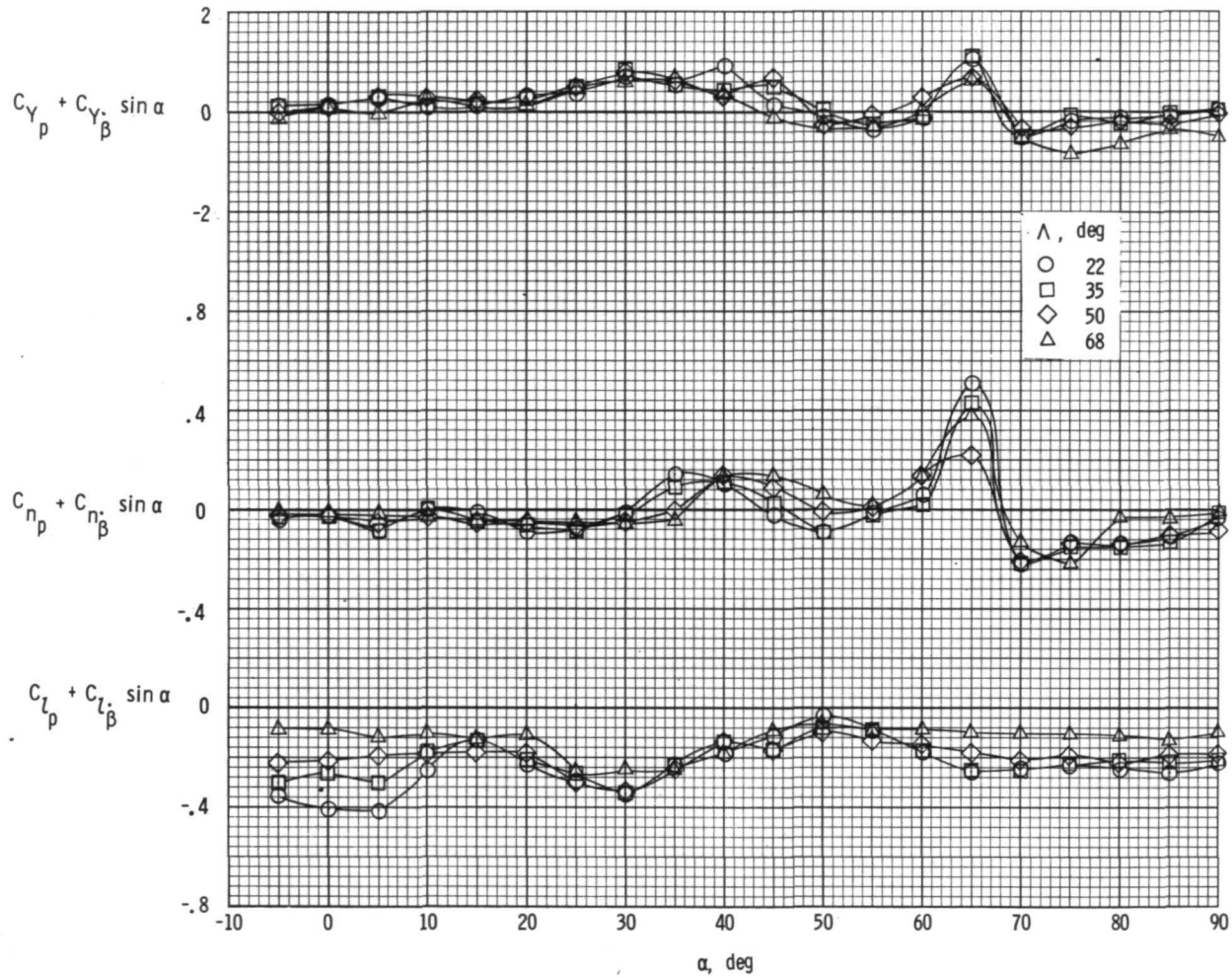

Figure 13.- Effect of wing sweep on the dynamic rolling derivatives. $\Delta\phi = \pm 5^{o}$; $i_t = 0^{o}$; $k = 0.305$.

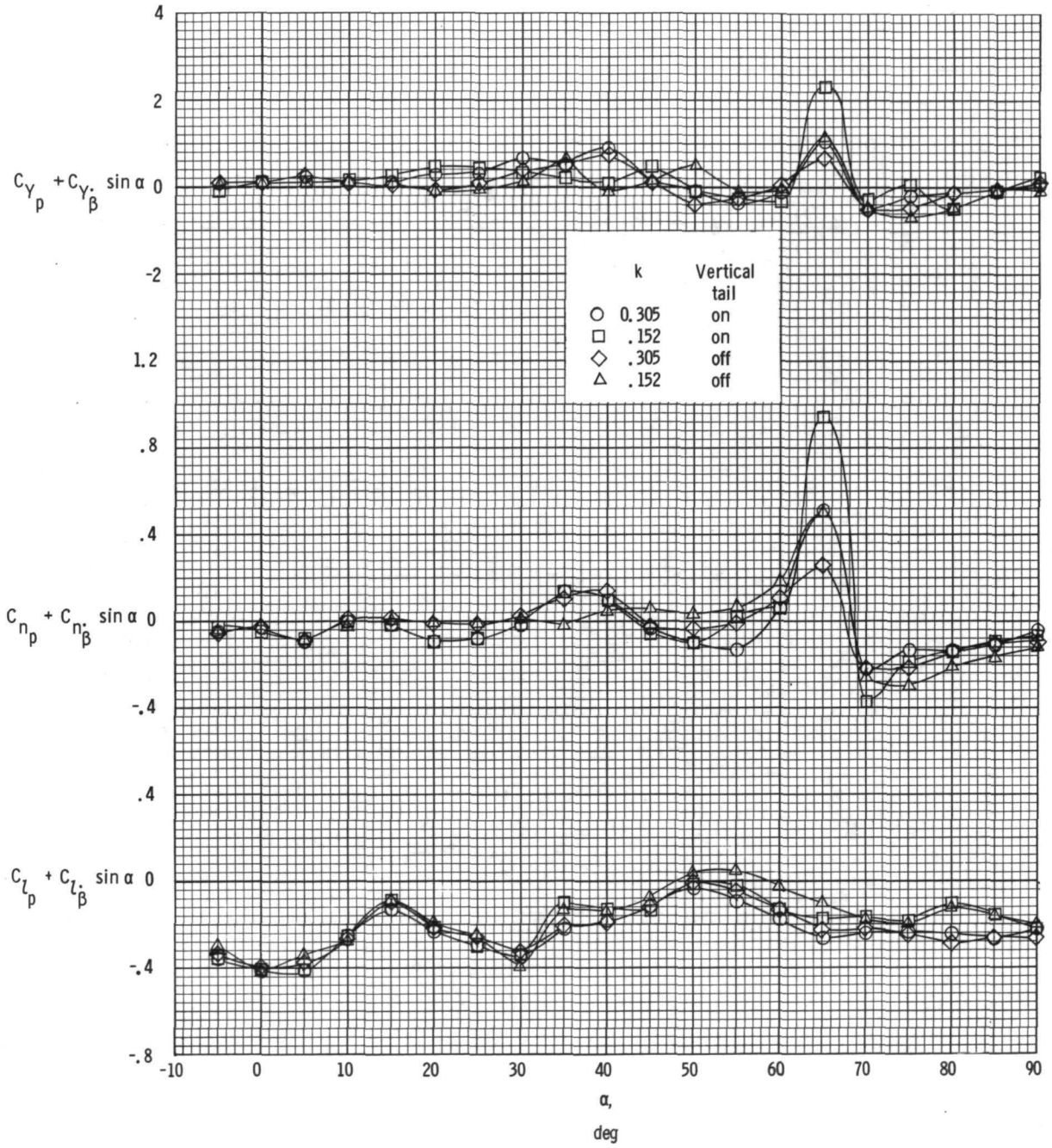

(a) $\Lambda = 22^{\circ}$.

Figure 14.- Effects of frequency and vertical tails on the dynamic rolling derivatives. $\Delta\phi = \pm 5^{\circ}$.

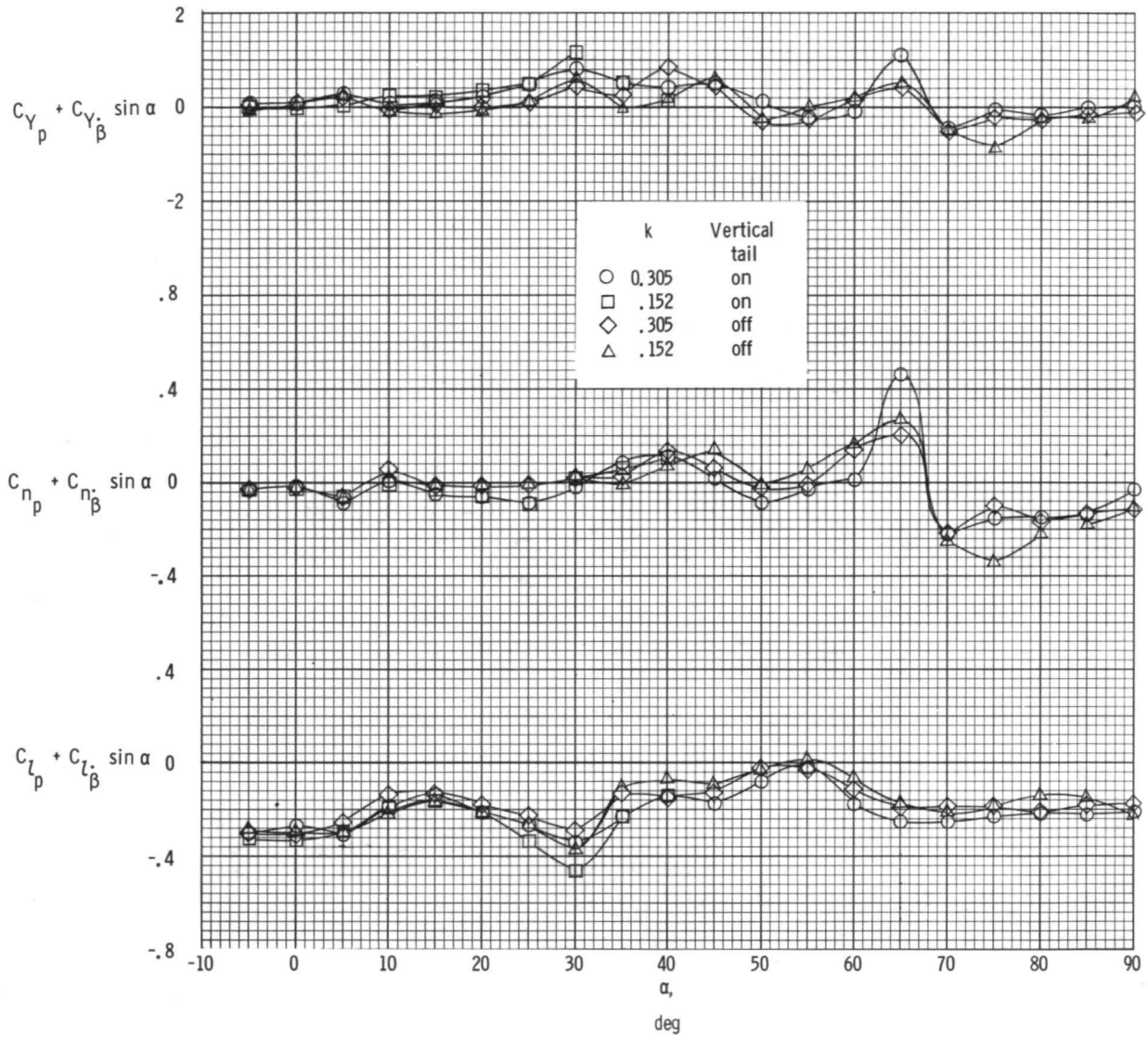

(b) $\Lambda = 35^{o}$.

Figure 14.- Continued.

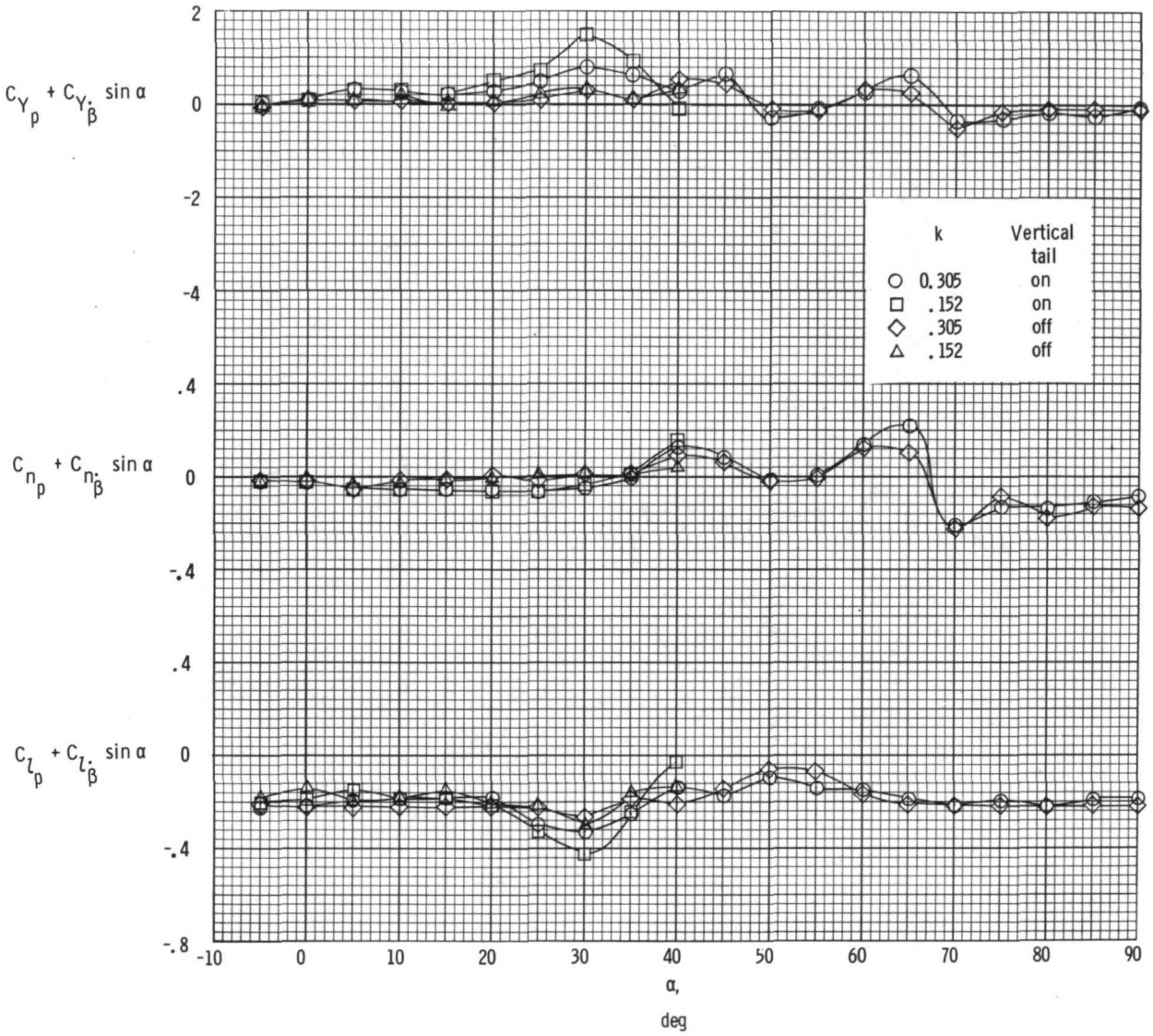

(c) $\Lambda = 50^{\circ}$.

Figure 14.- Continued.

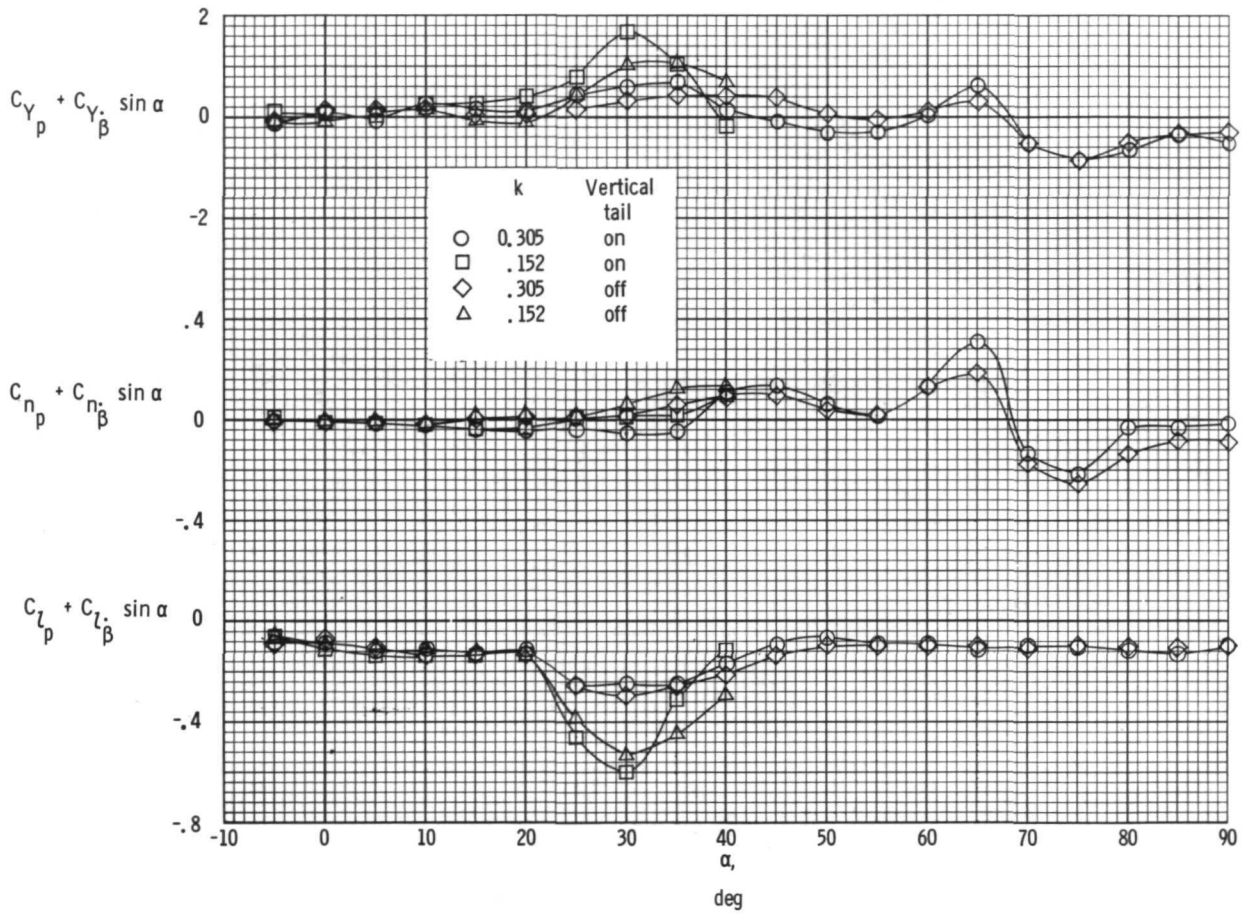

(d) $\Lambda = 68^{\circ}$.

Figure 14.- Concluded.

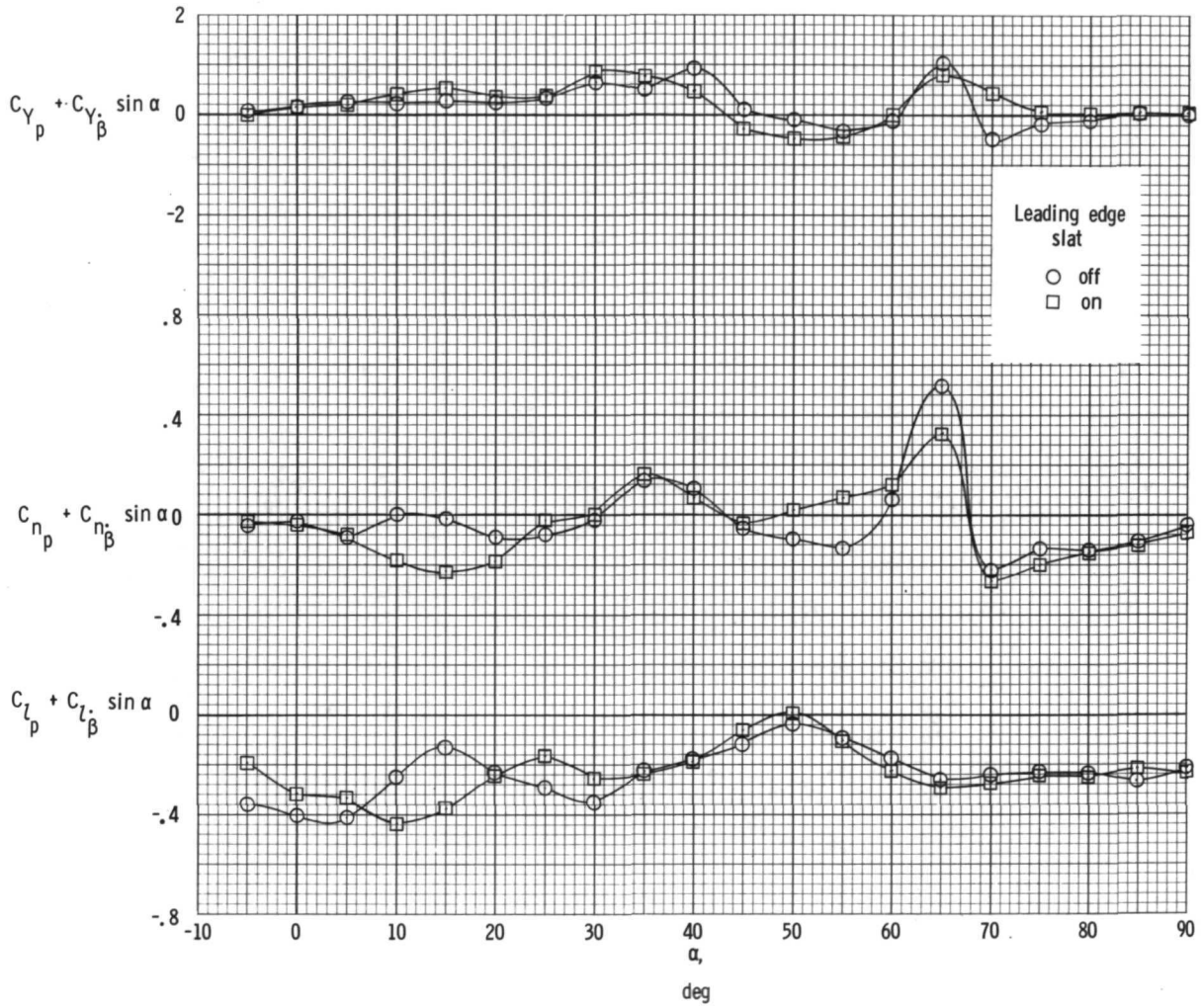

Figure 15.- Effect of leading-edge slats on the dynamic rolling derivatives. $\Lambda = 22^{o}$; $\Delta\phi = \pm 5^{o}$; $i_t = 0^{o}$; $k = 0.305$.

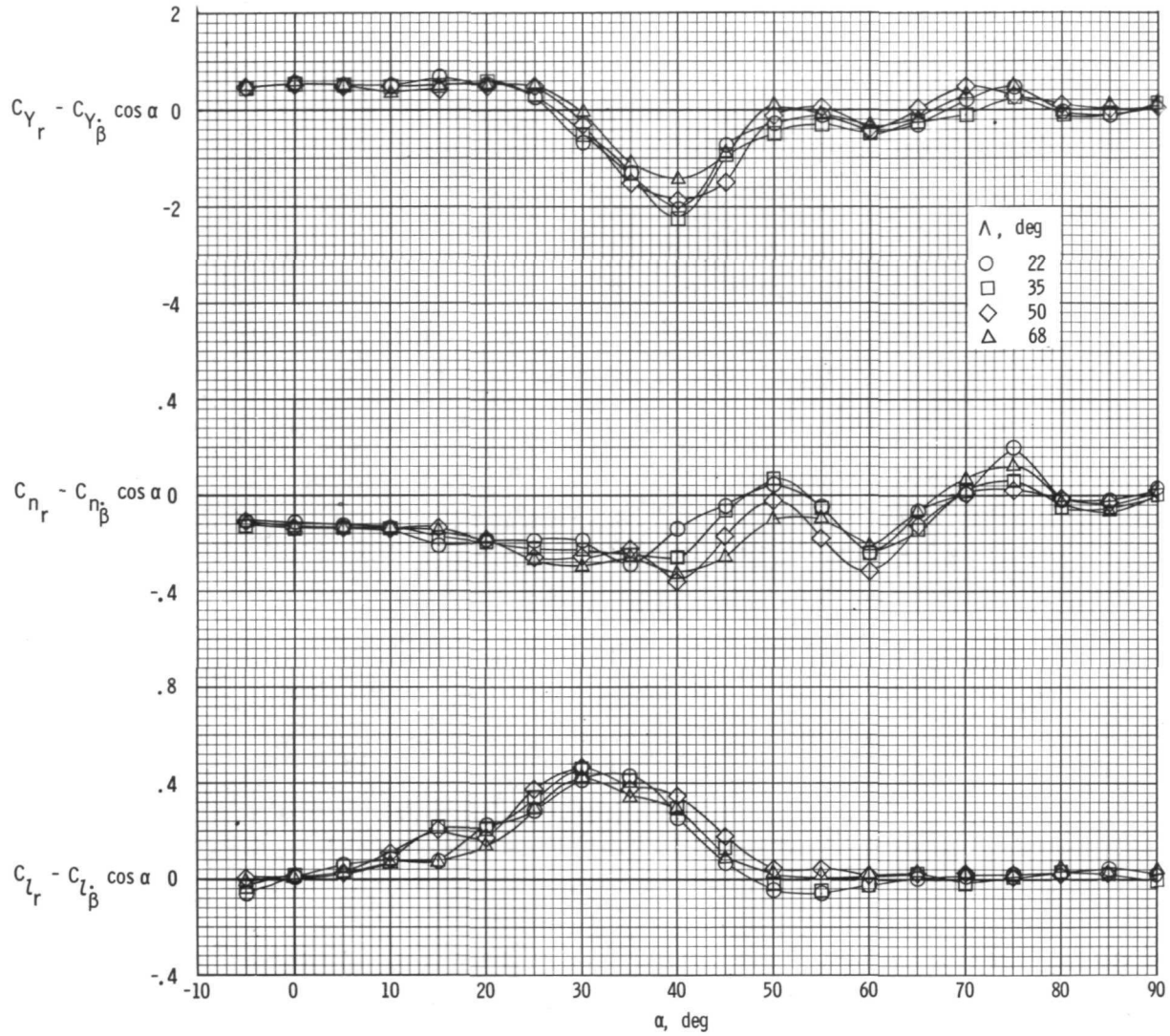

Figure 16.- Effect of wing sweep on the dynamic yawing derivatives. $\Delta\psi = \pm 5^{o}$; $i_t = 0^{o}$; $k = 0.305$.

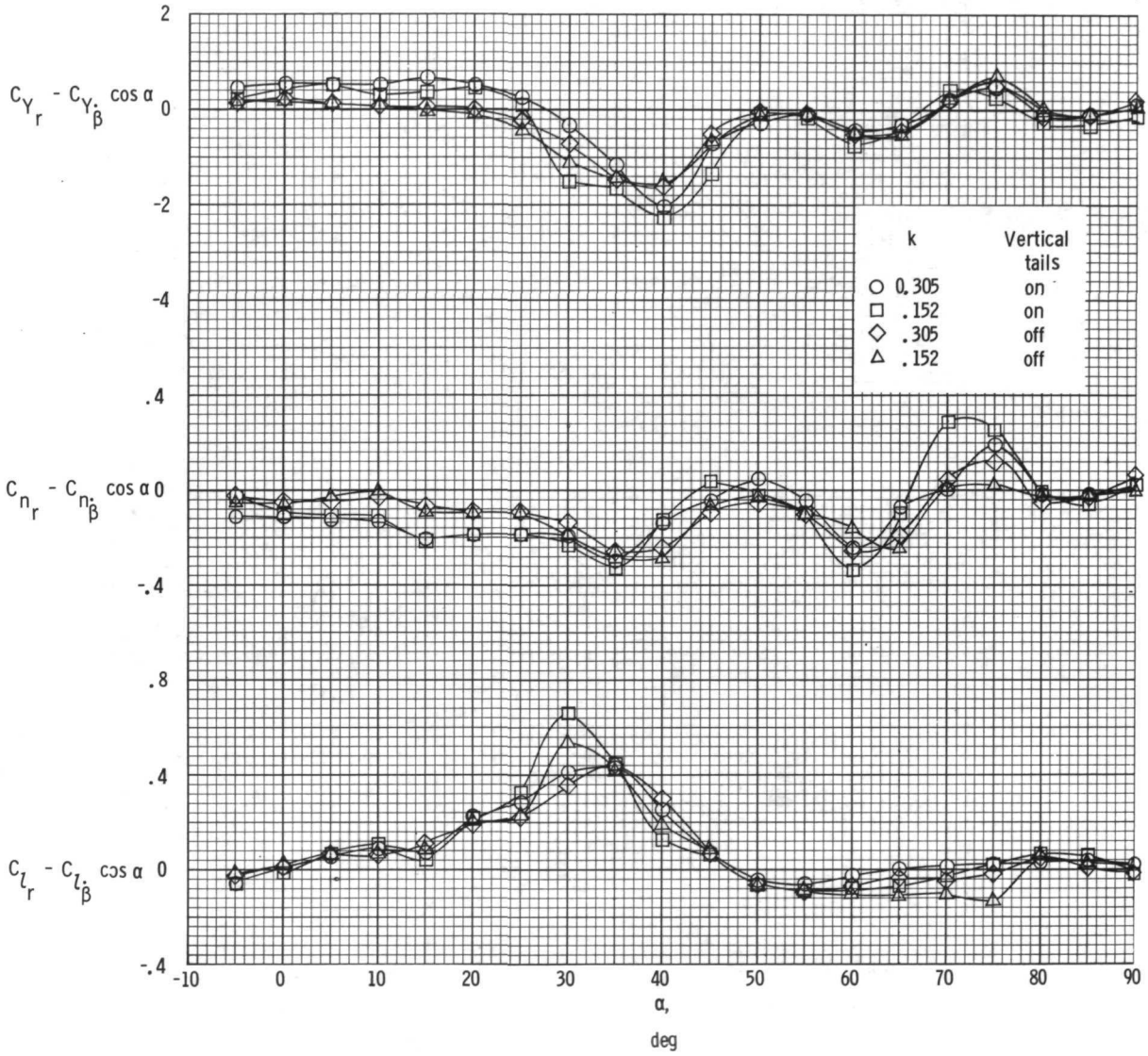

(a) $\Lambda = 22^{\circ}$.

Figure 17.- Effects of frequency and vertical tails on the dynamic yawing derivatives. $\Delta\psi = \pm 5^{\circ}$.

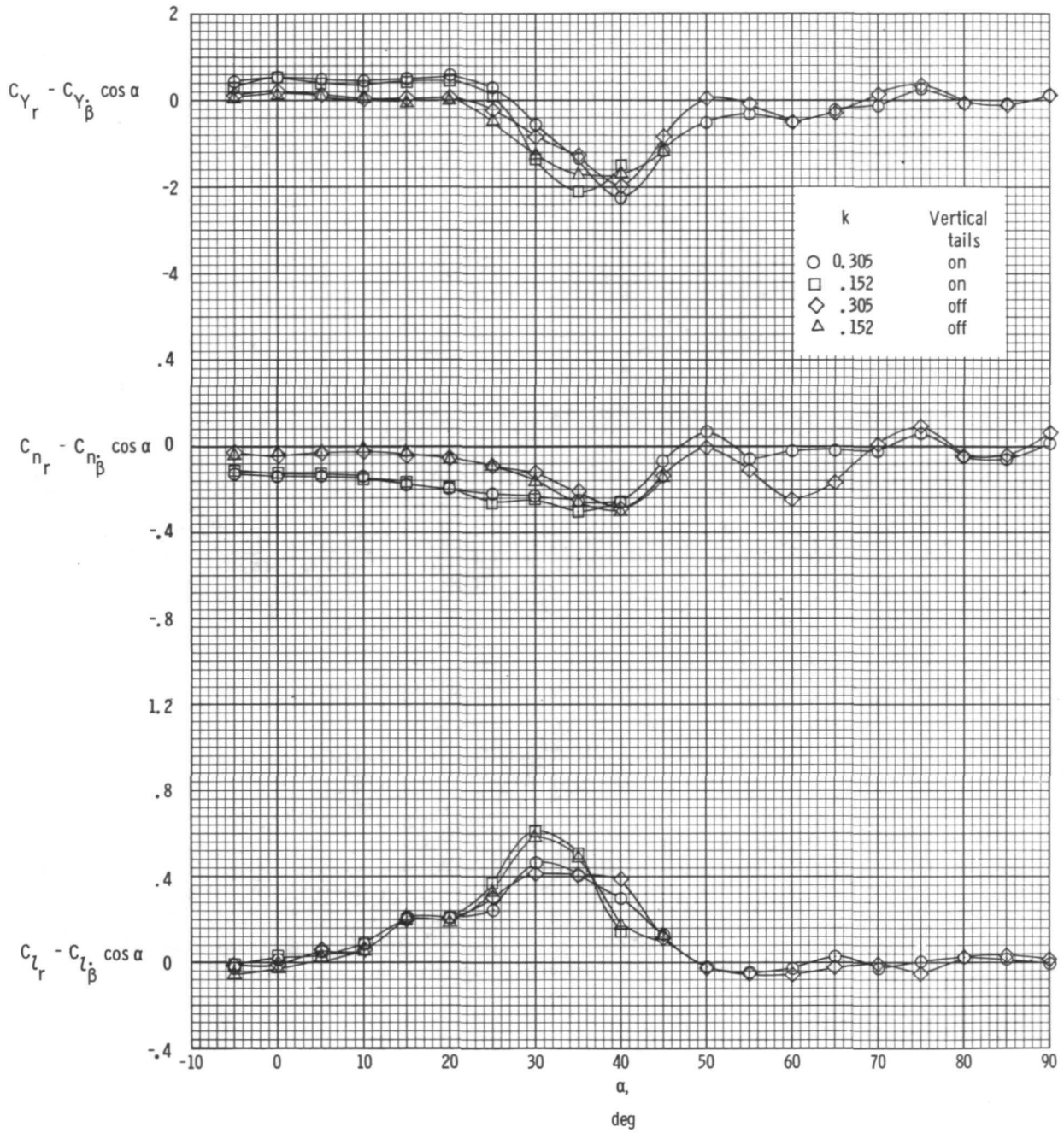

(b) $\Lambda = 35^{o}$.

Figure 17.- Continued.

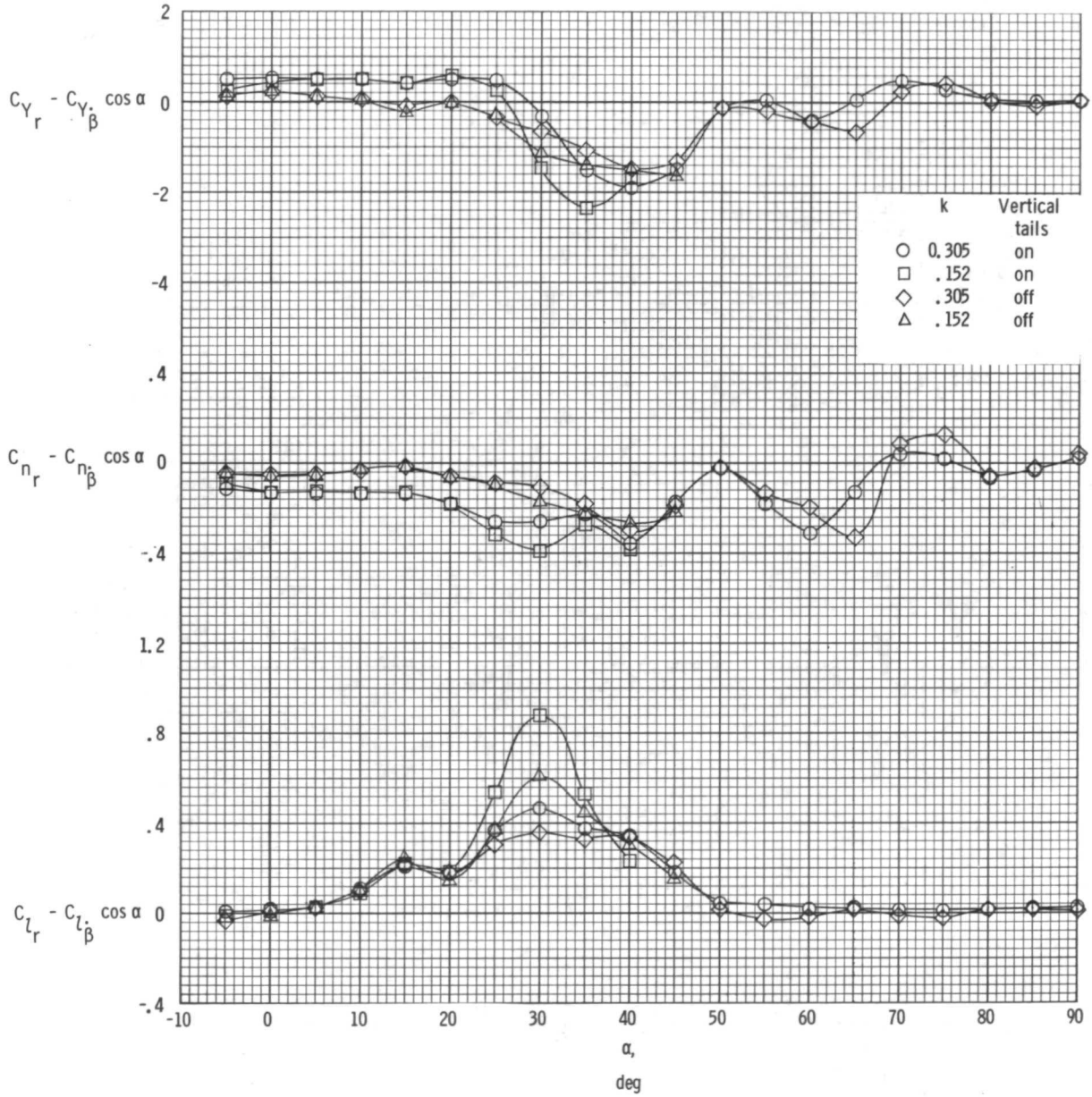

(c) $\Lambda = 50^{o}$.

Figure 17.- Continued.

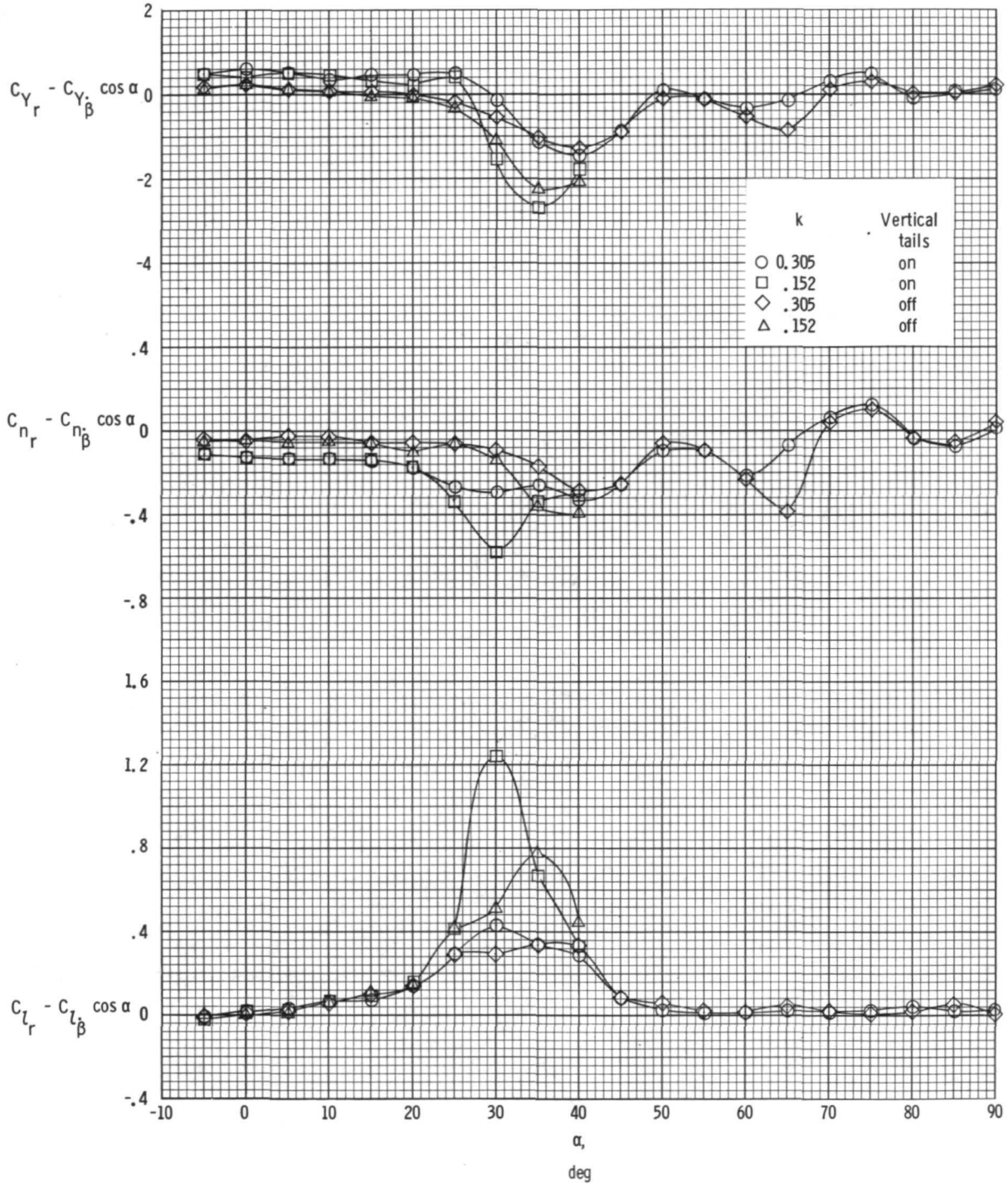

(d) $\Lambda = 68^{\circ}$.

Figure 17.- Concluded.

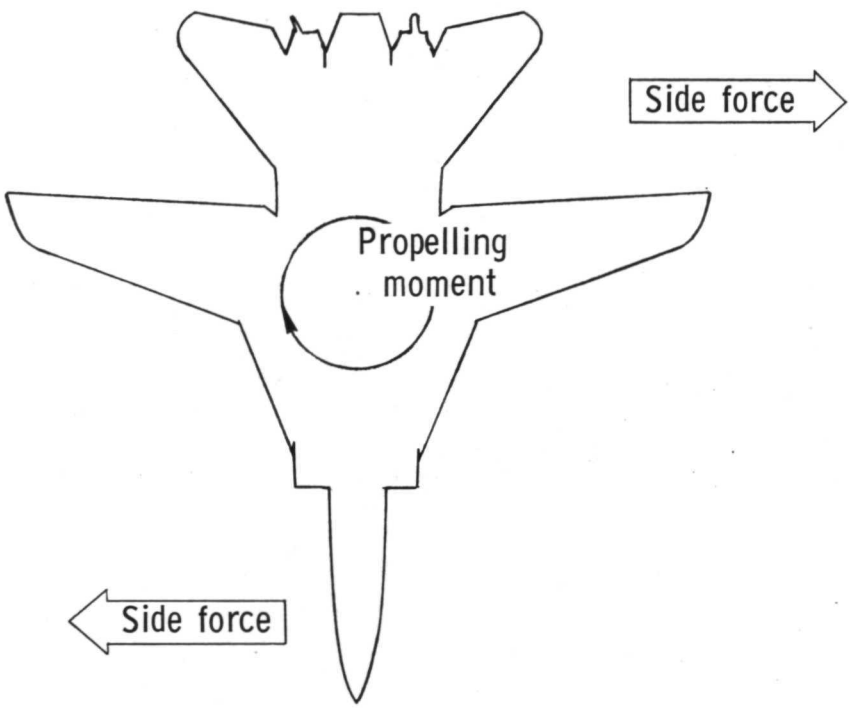

Figure 18.- Assumed relationship between side force and yawing moment during spin to right.

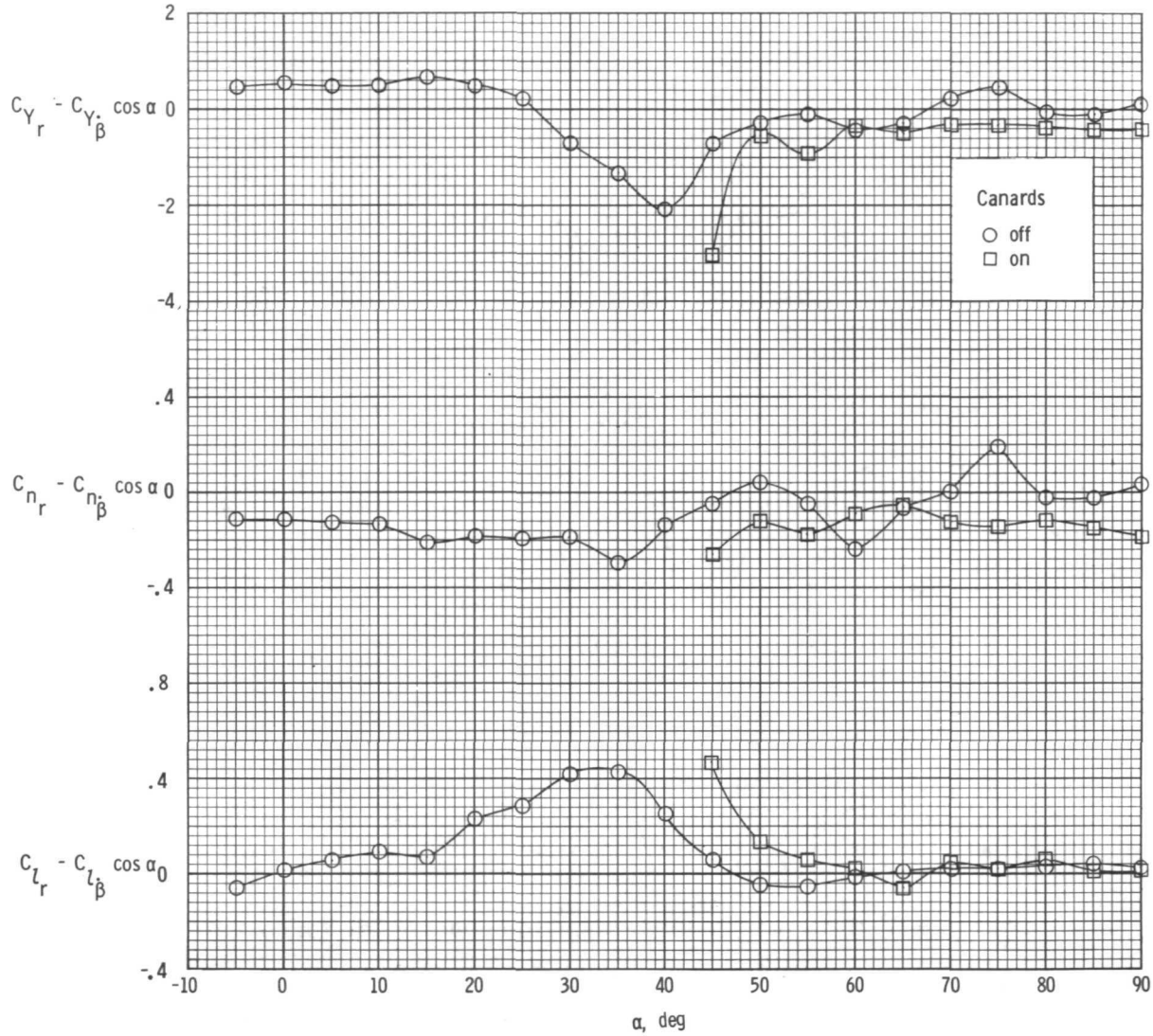

Figure 19.- Effect of canards on the dynamic yawing derivatives. $\Lambda = 22^{o}$; $\Delta\psi = \pm 5^{o}$; $i_t = 0^{o}$; $k = 0.305$.

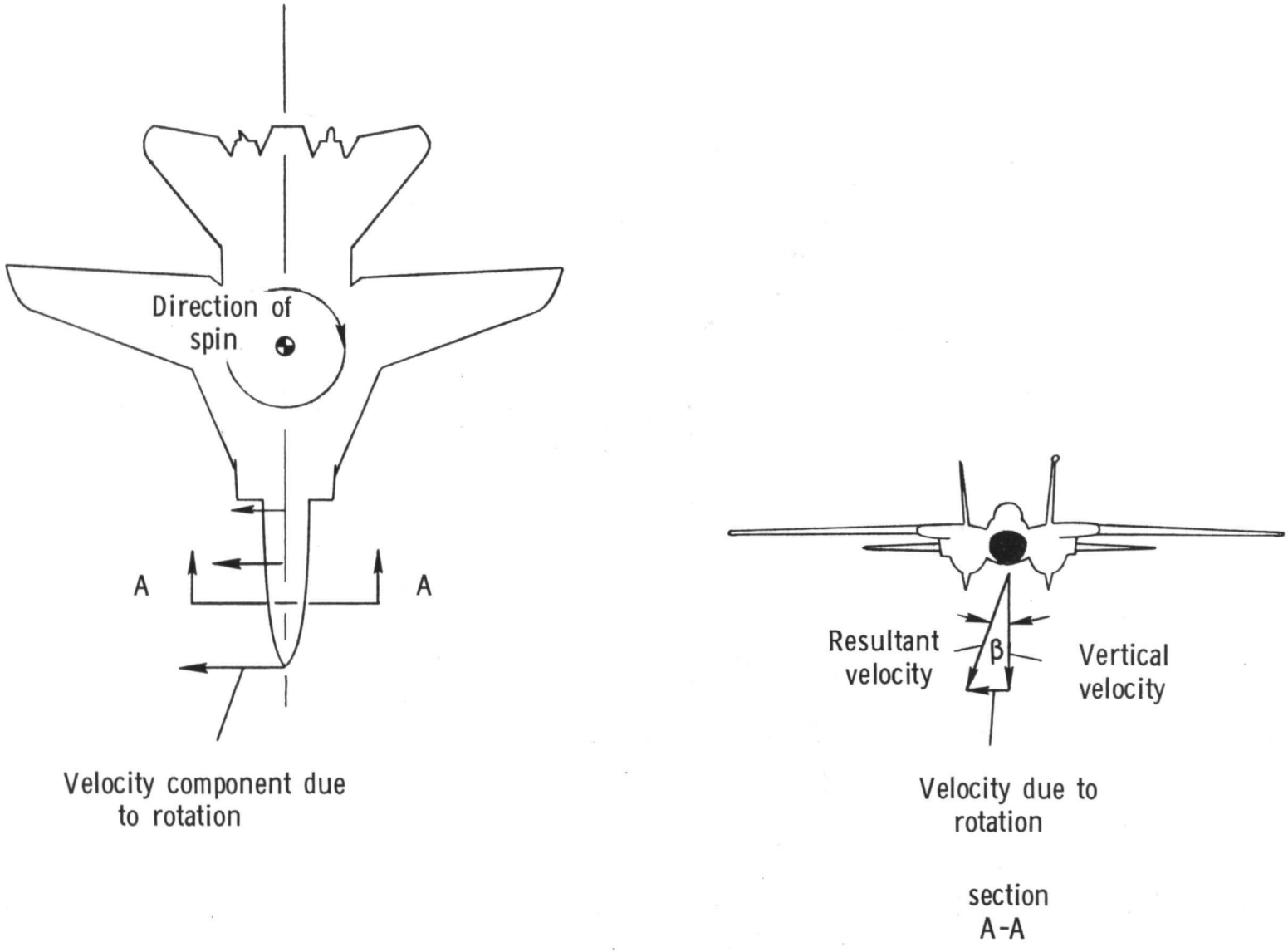

Figure 20.- Sideslip angle generated at nose of airplane during a right spin at 90° angle of attack.

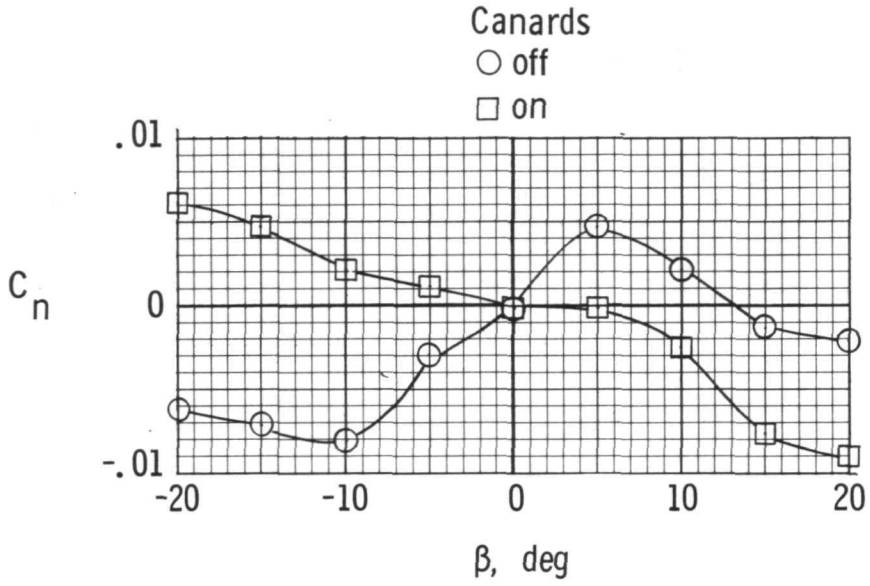

Figure 21.- Variation of yawing-moment coefficient with angle of sideslip. $\alpha = 85^{o}$; $\Lambda = 22^{o}$.

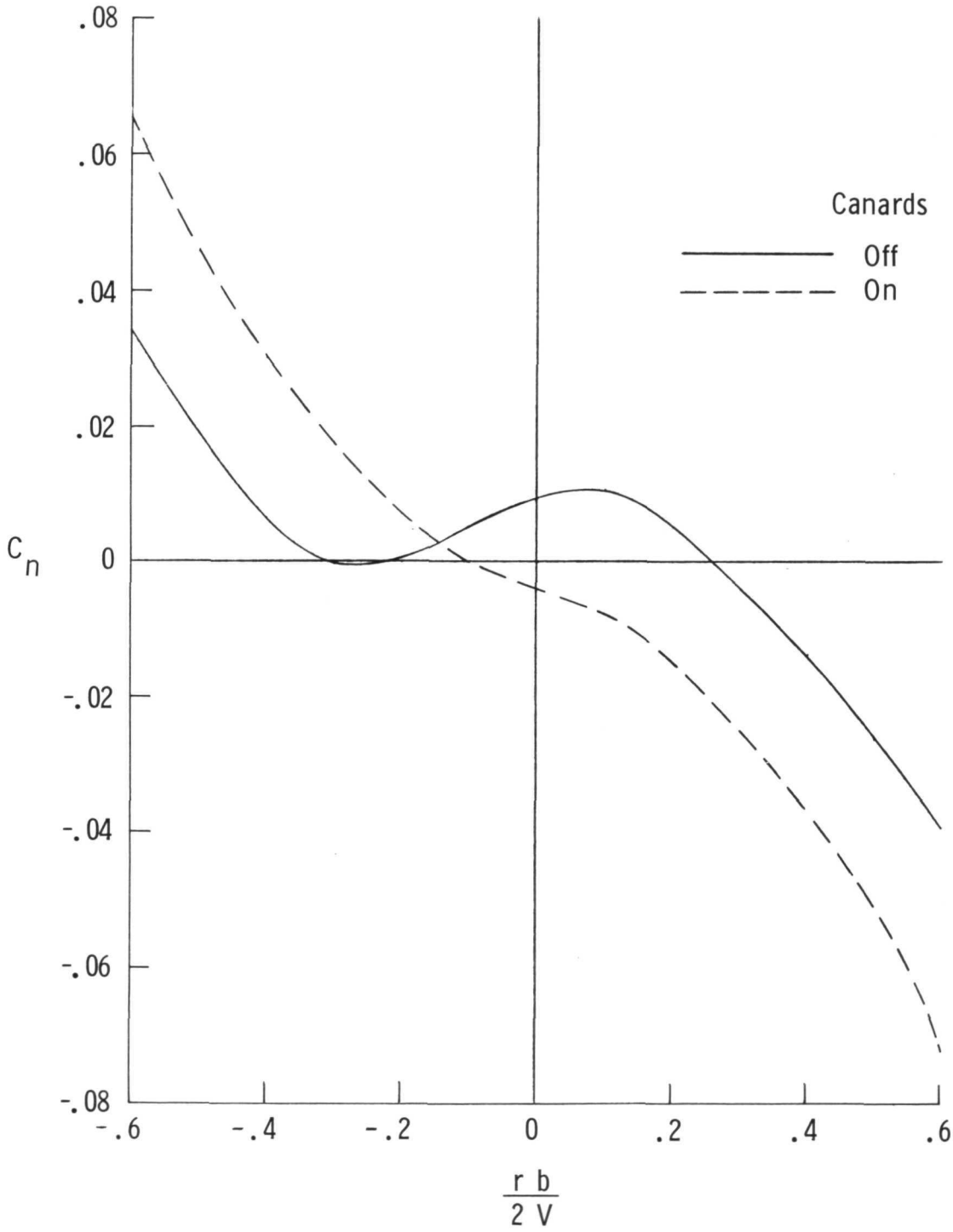

Figure 22.- Variation of yawing-moment coefficient with rate of rotation in a spin. $\Lambda = 22^{o}$; $\alpha = 85^{o}$; $i_t = 0^{o}$.

NATIONAL AERONAUTICS AND SPACE ADMISTRATION
WASHINGTON, D.C. 20546

OFFICIAL BUSINESS
PENALTY FOR PRIVATE USE $300

FIRST CLASS MAIL

POSTAGE AND FEES PAID
NATIONAL AERONAUTICS AND
SPACE ADMINISTRATION

U.S.MAIL

NASA 451

POSTMASTER: If Undeliverable (Section 158 Postal Manual) Do Not Return

"The aeronautical and space activities of the United States shall be conducted so as to contribute . . . to the expansion of human knowledge of phenomena in the atmosphere and space. The Administration shall provide for the widest practicable and appropriate dissemination of information concerning its activities and the results thereof."

— NATIONAL AERONAUTICS AND SPACE ACT OF 1958

NASA SCIENTIFIC AND TECHNICAL PUBLICATIONS

TECHNICAL REPORTS: Scientific and technical information considered important, complete, and a lasting contribution to existing knowledge.

TECHNICAL NOTES: Information less broad in scope but nevertheless of importance as a contribution to existing knowledge.

TECHNICAL MEMORANDUMS: Information receiving limited distribution because of preliminary data, security classification, or other reasons.

CONTRACTOR REPORTS: Scientific and technical information generated under a NASA contract or grant and considered an important contribution to existing knowledge.

TECHNICAL TRANSLATIONS: Information published in a foreign language considered to merit NASA distribution in English.

SPECIAL PUBLICATIONS: Information derived from or of value to NASA activities. Publications include conference proceedings, monographs, data compilations, handbooks, sourcebooks, and special bibliographies.

TECHNOLOGY UTILIZATION PUBLICATIONS: Information on technology used by NASA that may be of particular interest in commercial and other non-aerospace applications. Publications include Tech Briefs, Technology Utilization Reports and Technology Surveys.

Details on the availability of these publications may be obtained from:

SCIENTIFIC AND TECHNICAL INFORMATION OFFICE

NATIONAL AERONAUTICS AND SPACE ADMINISTRATION

Washington, D.C. 20546